MICROSTRUCTURAL AND MECHANICAL PROPERTY CHANGES IN ION IRRADIATED TUNGSTEN

A Thesis

by

MICHAEL JUSTINN GENERAL

Submitted to the Office of Graduate Studies of
Texas A&M University
in partial fulfillment of the requirements for the degree of

MASTER OF SCIENCE

Approved by:

Chair of Committee,	Lin Shao
Committee Members,	Sean McDeavitt
	Xinghang Zhang
Intercollegiate Faculty Chair,	Ibrahim Karaman

May 2013

Major Subject: Materials Science and Engineering

ABSTRACT

Sustainable fusion power is within reach; however, more research is needed in the field of material science and engineering. One critical component of a fusion reactor is the plasma facing material. Very little literature exists on the sustainability of tungsten as a plasma facing material (PFM). During operation, PFM must withstand harsh conditions with combined effects from high temperature, mechanical stress, irradiation, transmutation, and the production of hydrogen (H) and helium (He) from nuclear reactions. Therefore, this thesis will focus on co-implantation of H and He into tungsten to investigate the mechanical and microstructural material response.

For the first part of this study, Molecular Dynamics (MD) was used to qualitatively understand defect migration and mechanical property changes in tungsten. A Brinell hardness test was simulated using MD in tungsten to study the dependence on void size and void density hardness. It was found that hardness changes vary as the square root of the void size and void density. Also the movement of dislocations and its interaction with voids were investigated.

For the second part of the study, H and He were co-implanted into tungsten to look at the mechanical and microstructural changes. Hardness changes were measured using a nano-indenter ex-situ on post-irradiated specimen. Results show that the hardness of tungsten after co-implantation is proportional to the square root of the fluence. Additionally, the microstructure of irradiated tungsten samples was investigated by using a Transmission Electron Microscope (TEM). It was observed that the defect microstructure in tungsten, after co-implantation, is quite complex, with a number of

intriguing features, such as the presence of the nano-bubbles and dislocation loops. Also it was observed that there was an effect that H has on the nucleation of He nano-bubbles. The results from this work suggest that the effect of co-implanting H and He into tungsten is crucial to fully understand its viability as a PFM.

DEDICATION

To my parents and my friends, thank you for your love, care, and support through the years.

ACKNOWLEDGEMENTS

I would like to acknowledge Dr. Shao for his help and guidance during my time at Texas A&M University. I would like to also acknowledge my committee members, Dr. McDeavitt and Dr. Zhang for their help and support. I would also like to extend my gratitude to, D. Chen, Dr. Aikaliveya, L. Price, C. C. Wei, R. Vega, M. A. Myers, J. Wallace, and F. Edmiston, E. Hwang who helped me with this thesis.

NOMENCLATURE

b	Burgers Vector
BCC	Body-Centered Cubic
Be	Beryllium
CFC	Carbon Fiber Reinforced Composite
E	Energy
EAM	Embedded-atom Method
eV	Electron Volt
FIB	Focused Ion Beam
He	Helium
H	Hydrogen
H_b	Brinell Hardness
H_v	Vickers Hardness
INLO	In-situ Lift Out
ITER	International Thermonuclear Experiment Reactor
LAMMPS	Large-scale Atomic/Molecular Massive Parallel Simulator
m	Meter
MD	Molecular Dynamics
Pa	Pascal
PFM	Plasma Facing Material
PKA	Primary Knock-on Atom
ps	Picoseconds

R	Range
R_p	Projected Range
SEM	Scanning Electron Microscope
TEM	Transmission Electron Microscope
V	Vacancy

TABLE OF CONTENTS

LIST OF FIGURES

LIST OF TABLES

1. INTRODUCTION

The promise of a sustainable fusion power plant has captivated the human race for decades. However, to make this vision a reality, a substantial amount of engineering and research must be performed, especially in the field of material science. For example, one of the most critical components for a fusion reactor is the PFM. Such materials must withstand incredibly harsh conditions, with combined effects from high temperatures, mechanical stresses, and large doses of radiation over an extended period of time. These components must maintain their structural integrity, and, thus, the development of materials which can tolerate this environment is essential.

The International Thermonuclear Experimental Reactor (ITER) announced the use of tungsten for portions of the reactor "first-wall" [1]. Figure 1.1 is an illustration of the ITER showing along with material selections for major components. The main PFM will be comprised of Beryllium (Be), tungsten, and carbon fiber-reinforced carbon composite (CFC). Beryllium will be used for the main wall coating, and tungsten and CFC will be used for the divertor. The divertor shown at the bottom of Fig 1.1 in the ITER fusion reactor design is a critical component due because of its purpose to remove and control the build of the transmutation of fusion by-products. This means that the divertor will be exposed to the highest flux of plasma, and, thus, have the highest levels of radiation and heat [2]. Safe reactor operation requires complete knowledge of divertor properties under extreme conditions. Therefore, this study will focus on the viability of tungsten as a PFM.

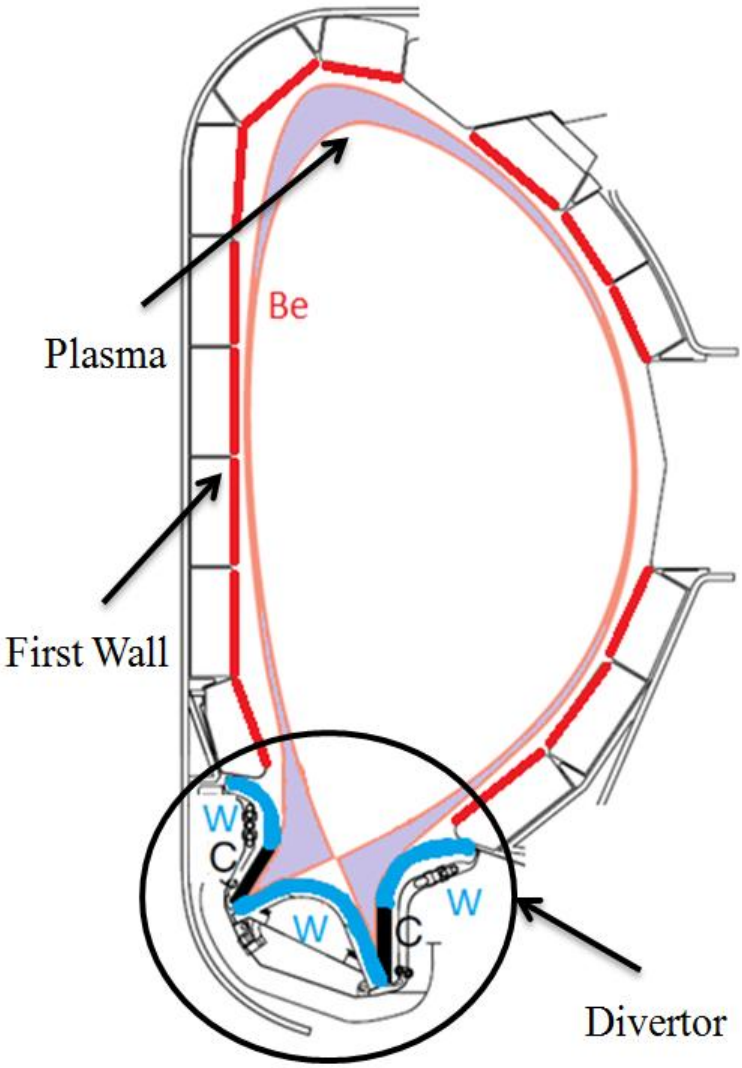

Figure 1.1: An illustration of the proposed materials used for the PFM of the ITER reactor design.

Over the past decade, various researchers from around the world have studied tungsten's viability as a PFM. Tungsten is a strong PFM candidate due to its high melting point and low sputtering yield. A large body of work exists on the diffusion of H and He in tungsten, as well as the effect of H and He irradiation individually on the

near surface region. A few studies have examined the effect of implanting H and He into tungsten [3-8]; however, to our knowledge, none have investigated the mechanical properties and/or microstructural changes due to co-implantation.

Therefore, this thesis will focus on expanding this body of knowledge and examine the change in mechanical properties of tungsten under the co-implantation of He + H and implantation of He. This study has been broken into two distinct sections to better illustrate and characterize this phenomenon.

The first part of this study will observe the changes in mechanical properties of tungsten by utilizing Molecular Dynamics (MD) simulations. By examining the results of these simulations, one can gain a better understanding of what mechanisms cause the change in the mechanical properties of tungsten. The simulation will recreate a nano-indent into tungsten for which the hardness can be extracted. The next step is to place voids in the simulation, and look at the dependency of void size and void density, and how these two parameters affect the hardness of tungsten. Also to understand the movement of dislocations and interaction it has with voids.

The second part of this study will examine the experimental results of H and He co-implanted tungsten and measure its mechanical properties. Next, identify the microstructural changes that may have occurred in the ion irradiation process and tries to relate that back to the mechanical property changes. Initially, for this experiment, the samples will be bombarded with H and He, the most common ion species in fusion plasma. After the ion irradiation process, these samples will be mechanically tested by

using a nanoindenter. Then look at the cross-sectional TEM of these samples, where the microstructural changes can be analyzed.

2. BACKGROUND THEORY

This section presents fundamental principles, of ion-solid interactions, such concepts are interatomic potentials, binary elastic collisions, ion stopping, electronic and nuclear stopping, damage cascades, and radiation damage. Also presented are macro-level principles of mechanical properties and the impact of dislocations, radiation damage, and the presence of foreign species, and their effect on the hardness of the material. Such concepts are necessary to understand the data presented herein. The aforementioned topics will be discussed in the following sub-sections.

2.1 Ion Solid Interaction

An ion-solid interaction is the physical processes that are a result from the collision of energetic ions with matter. To understand this concept, one must understand the principles of interatomic potentials, binary elastic collision, range, ion stopping, and displacement spike.

2.1.1 Interatomic Potential

The interatomic potential between two atoms gives rise to almost all physical phenomena, such as the heat capacity, pressure, the strength of a solid, and the viscosity of a liquid. Most importantly, it greatly affects the scattering probability of an ion solid interaction. The simplest way of understanding interatomic potentials is to first look at the electrostatic potential V(r) between two point charges with a charge e separated by a distance r, given by

$$V(r) = \frac{e^2}{r}. \tag{2.1}$$

The potential from Eqn. 2.1, is related to the force F(r) by Eqn. 2.2, given by

$$F(r) = -\frac{d}{dr}[V(r)]. \tag{2.2}$$

One way of conceptualizing the interatomic potential of a pair of atoms is by bringing the atoms, from an infinite separation distance, to their equilibrium. The total amount of work required to assemble such a configuration is the interatomic potential energy.

There are more sophisticated interatomic potentials which provide more accurate explanations for complex systems, such as hard-sphere, square-well, inverse power, and the Lennar-Jones potentials. These different models provide varying levels of detail about how atoms interact with one other.

Previously, it was stated that many physical properties such as elastic properties and thermal properties arise as a result of the interatomic potential between atoms. The modulus of elasticity is a function of the strength of the interatomic potentials between the atoms in a lattice. If an external force is exerted on a crystal, bond breaking will only occur if the potential barrier between atoms is overcome. The strength of these bonds is determined by the interatomic potential, and, thus, if the force exerted is less than the amount of energy needed to displace an atom from its original lattice site, the binding energies have not been exceeded. In other words, binding energy is the amount of energy needed for an atom to overcome the potential barrier and become mobile. The melting temperature of a material is a function of the depth of the potential well and directly related to the binding energy. It is generally known that, there is a linear relationship between the binding energy, the melting point, and the modulus of elasticity.

2.1.2 Binary Elastic Collision

For the following discussion, consider a two body collision, where the energy is conserved between the projectile and target. This type of collision is known as a binary elastic collision. The energy transfer between the two particles is a direct result of the conservation of energy and momentum. The collision is termed "elastic" since no energy is lost from the reaction. The governing kinematic given by Eqn. 2.4, 2.5, and 2.6, and illustrated in Fig. 2.1.

$$E_o = \frac{1}{2}M_1 v_o^2 = \frac{1}{2}M_1 v_1^2 + \frac{1}{2}M_2 v_2^2 \tag{2.4}$$

$$M_1 v_o = M_1 v_1 \cos\theta + M_2 v_2 \cos\phi \tag{2.5}$$

$$0 = M_1 v_1 \sin\theta - M_2 v_2 \sin\phi. \tag{2.6}$$

E_o is the initial energy of the projectile, M_1 is the mass of the projectile, M_2 is the mass of the target, v_o is the initial velocity of the projectile, v_1 is the velocity of the projectile, v_2 is the velocity of the target, and θ and ϕ are the scattering angles of the projectile and the target, respectively.

This model assumes that only two particles interact and that the excitation or ionization of electrons does not influence the collision dynamics. These assumptions are largely valid for the interactions discussed in this section.

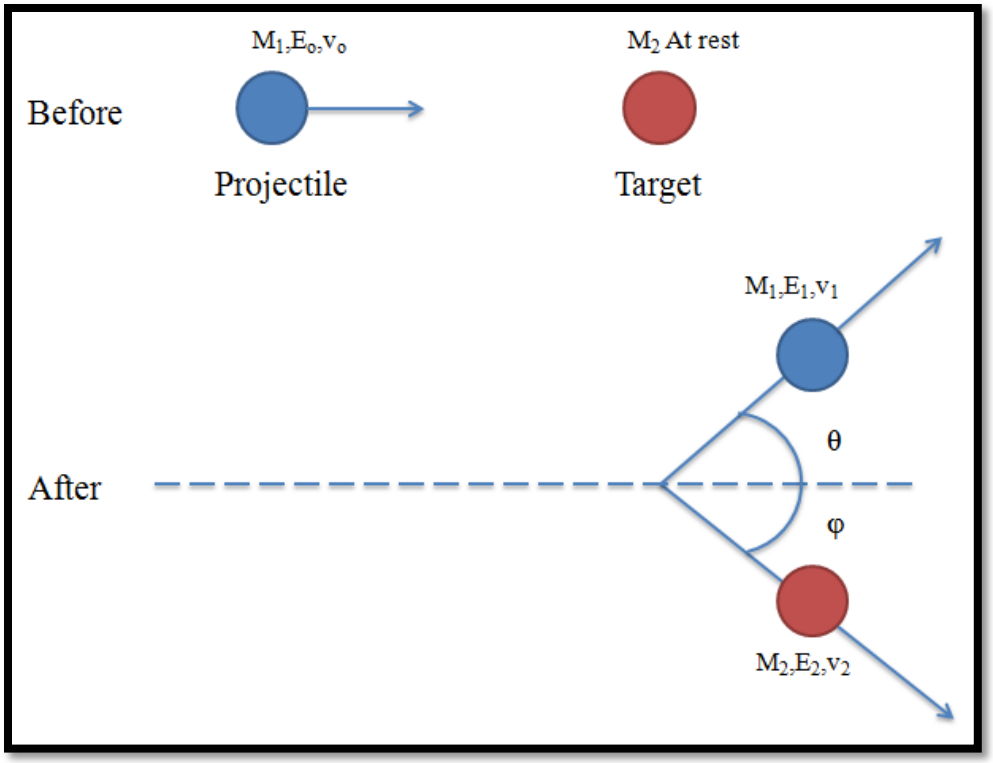

Figure 2.1 An illustration of a binary elastic collision governed by the kinematic Eqn. 2.4, 2.5, and 2.6. E_1 and E_2 is the new energy of the projectile and target after the collision, respectively.

2.1.3 Ion Range

As an ion travels through a solid, the atoms in that solid interact with the traveling ion through multiple collisions. For every collision, the ion is perturbed from its original course and sent off at a new trajectory. Through this collision, it parts some of the ion's energy to the target material. The path of the ion depends on several variables, such as the initial energy of the ion, the angle of incidence, and the target material. The total distance traveled by an ion is known as the range, R, which is given by Eqn. 2.7

$$R = \int_{E_0}^{0} \frac{1}{dE/dx} dE. \quad (2.7)$$

In the equation, E_o is the initial energy of the ion, and $\frac{dE}{dx}$ represents the energy loss over the distance traveled into the material. The $\frac{dE}{dx}$ term is often referred to as the stopping power of an ion traveling through the target material. However, $\frac{dE}{dx}$ is constantly changing based on the energy of the ion travelling through the target material.

The average distance perpendicular to the surface an ion travels is known as the projected range, R_p. Figure 2.2 illustrates the differences between of the range, R, and the projected range, R_p. Computer programs, such as, Stopping and Range of Ion in Matter (SRIM) can calculate the R_p of certain ions with a discrete energy into most materials.

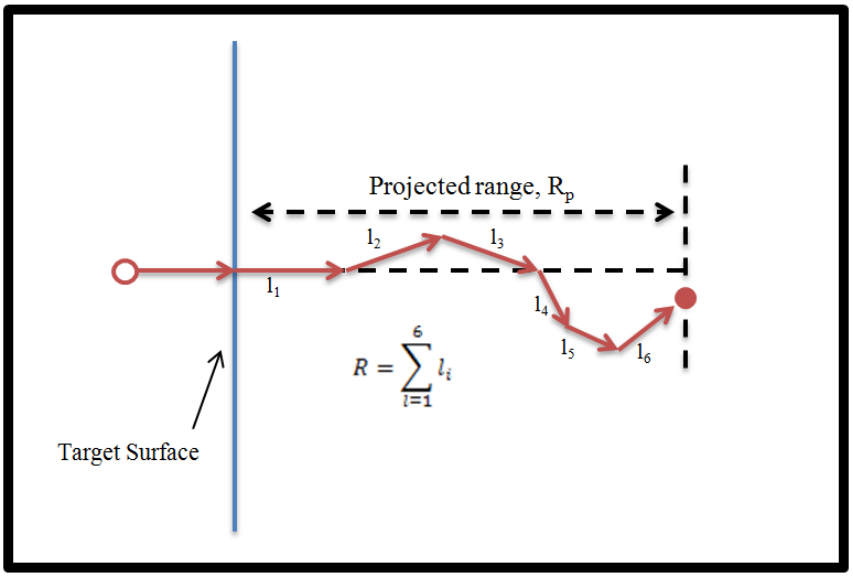

Figure 2.2: An ion traveling through a solid, as it illustrates the difference between the range of an ion verses the projected range.

2.1.4 Stopping Power

As an ion travels through a material, it deposits energy into the material through different interaction with the target material's electrons and nuclei. These two interactions are known as electronic stopping power and nuclear stopping power, respectfully. Electronic stopping is prevalent when the ion is traveling at high velocities and after each electronic interaction the ion transfers small amounts of energy into the target material. Nuclear stopping is prevalent when the ion is traveling at low velocities and the ion transfers large amount of energy. Each interaction depends on variables such as the ions mass, energy, and target material. The stopping power, $\frac{dE}{dx}$, is split between two components, $\frac{dE}{dx}_{nuclear}$, for interactions with the target nucleus, and $\frac{dE}{dx}_{eletronic}$,for interactions with the target electrons. Equation 2.8 is the stopping power split between the two components of nuclear stopping and electronic stopping.

$$\frac{dE}{dx} = \frac{dE}{dx}_{nuclear} + \frac{dE}{dx}_{eletronic} \tag{2.8}$$

Figure 2.3 illustrates the regions of dominate of nuclear stopping and electronic stopping as a function of the ion's velocity. Bohr suggested that based on the velocity and atomic number of the ion; there was a correlation to the number of ionizations as an ion travels through the target material. The correlation represents the effective ion charge fraction of the traveling ion, γ, seen from Eqn. 2.9,

$$\gamma = \frac{v}{v_o Z^{2/3}}. \tag{2.9}$$

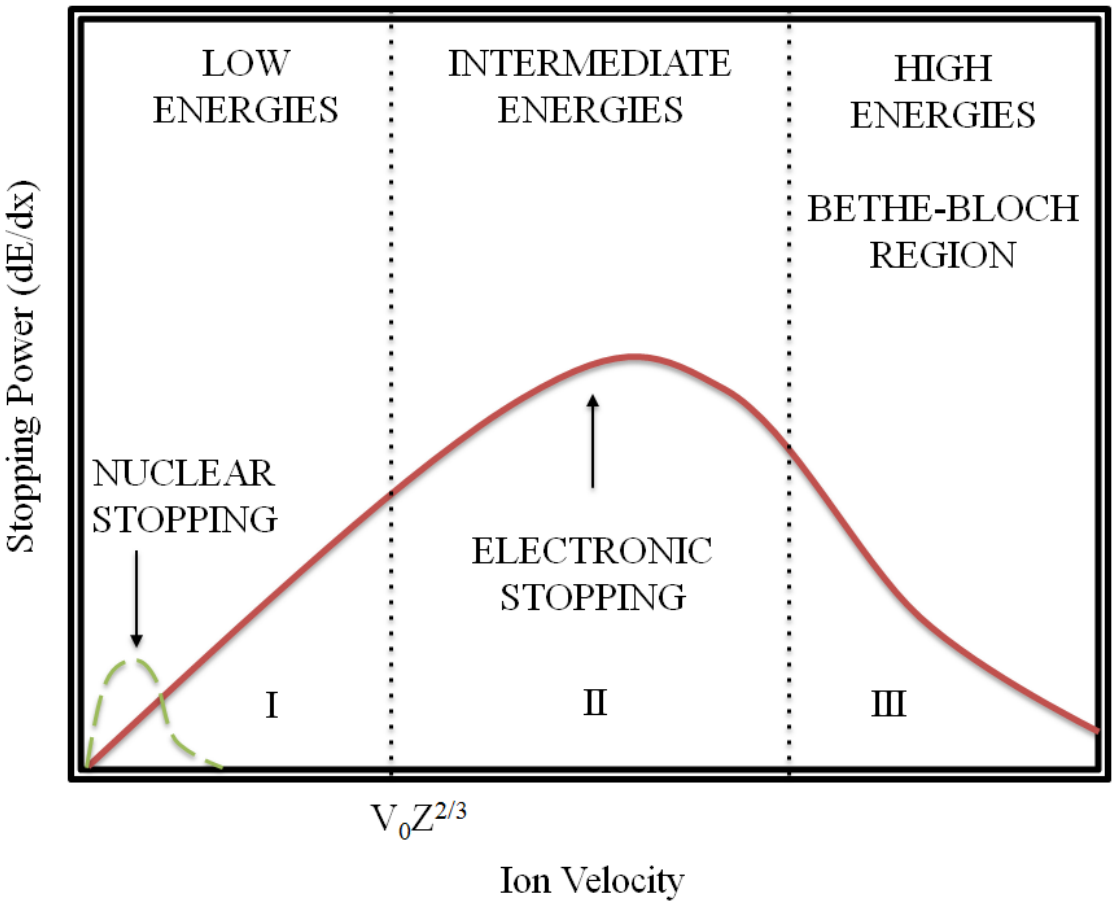

Figure 2.3: Illustrates the different regions for nuclear and electronic stopping power as a function of velocity.

In Eqn. 2.9, v is the velocity, Z is the atomic number of the ion and v_o is the Bohr velocity (2.2 x 10^6 m/s), the speed at which an electron orbits a nucleus. This correlation shows that for velocities of an ion greater than $v_o Z^{2/3}$, the ion is then considered to be stripped from all of its electrons, and all interaction of the traveling ion must occur through the electron clouds of the target material. For ion velocities less then $v_o Z^{2/3}$, the ion has all of its electrons and has a probability to interact with the target's nuclei.

Thereby, there exists a natural boundary between electronic stopping and nuclear stopping.

In the intermediate energies, seen in Fig.2.3 as region II, electronic stopping is the dominate interaction. For ion velocities greater than $v_o Z^{2/3}$, energy is transferred from the ion to the target atom from inelastic collisions with the target electrons. The electronic interaction that occurs transfers small amounts of energy from the ion to the target atoms, resulting in a slight perturbation of the original ion's path and a slight decrease in the ion's energy.

In the low energies, seen in Fig. 2.3 as region I, nuclear stopping is the dominate interaction. For ion velocities less then $v_o Z^{2/3}$, the ion is neutral and carries all of its electrons. The ion then has a high probability of interacting with the nuclei of the target material. By interacting with the nucleus, a large amount of energy is lost by a binary elastic collision and there is a significant angular deflection from the ion's original trajectory.

2.1.5 Displacement Spike

The amount of energy transferred to the target atom through elastic collisions is often enough to displace the target atom from its lattice site. The displaced atom now becomes a travelling particle through the medium and is often referred to as a Primary Knock-on (PKA). The PKA, if it has enough energy, could interact with the other target atoms in its vicinity, and "knock" those atoms from their lattice site. The displacement of the "knocked" atoms creates a cascade of displaced atoms in the target material. This

event is often referred to as damage cascades or displacement spikes. Figure 2.4 illustrates this idea of a displacement spike.

From the displacement spike, these atoms are originally displaced from their original spot, and create interstitials (when an atom occupies a site in a crystal structure where no atom is usually present), and vacancies (when no atom occupies a site in a crystal structure). These displacement spikes put the crystal lattice at an elevated energy state. In order to relax the crystal lattice to a lower energy state, the knocked atoms will migrate back towards the vacancies created by the PKA and subsequent knocked atoms.

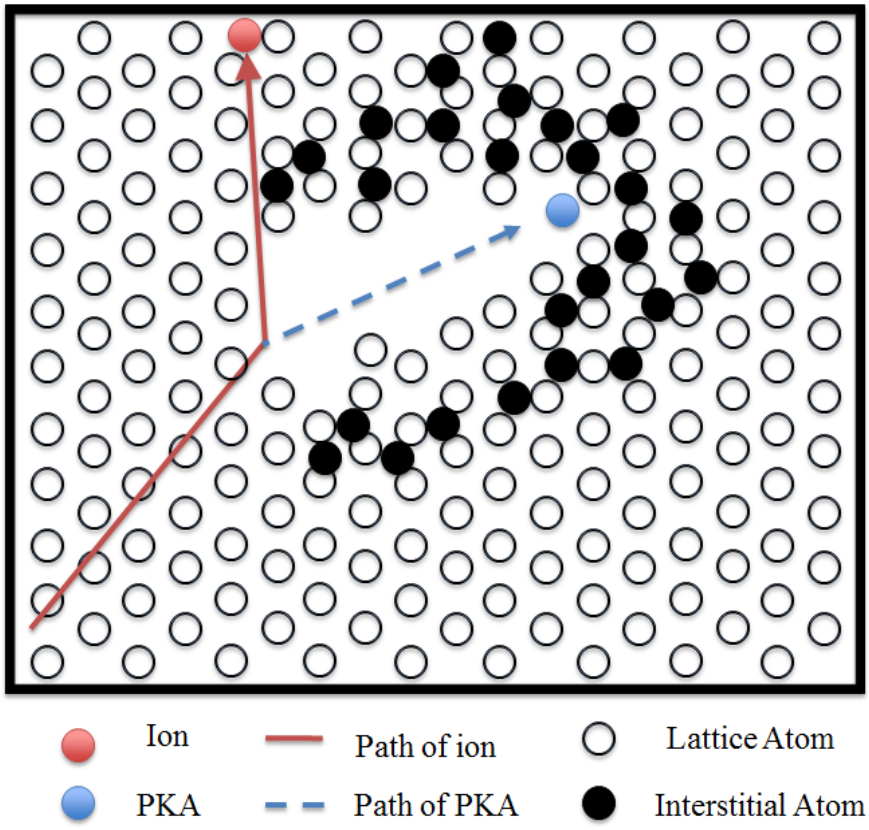

Figure 2.4: Illustrates when an ion interacts with one of the lattice atoms and creates a displacement spike.

However, since the atoms that were displaced might not have enough energy to go back to its original position, they will remain as an interstitial, thereby also creating a vacancy. Displacement spikes behind several interstitials and vacancies in the crystal lattice. These types of disturbances can lead to the production of defects. These defects have an effect on the mechanical properties of the material and will be discussed in the next section.

2.2 Mechanical Properties

In order to understand the effects that radiation has on materials, it is important to have a macro level understanding of mechanical properties. In this section, dislocations, dislocation migration, radiation damage, and the effects it has on the materials hardness will be discussed.

The hardness of a material is best described as the resistance to change in its shape when a force is applied on it. The hardness of a material is largely determined by the strength of the atomic bonds, or the interatomic potential. However, the crystal structure might contain irregularities such as point defects and line defects. These defects put a strain on the atomic bonds, thus changing the hardness of the material. A point defect is either a vacancy or an interstitial atom in the crystal structure. A line defect is an irregularity that exists in a misalignment of a plane of atoms in the crystal structure. Line defects are also known as dislocations.

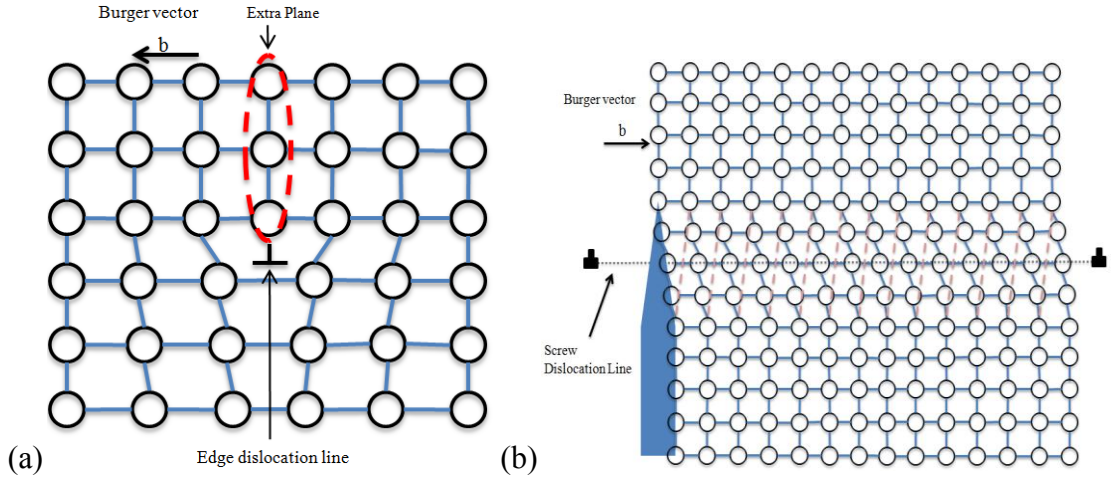

Figure 2.5: An example of two line defects, (a) an edge dislocation and (b) a screw dislocation.

A dislocation is a crystallographic defect within a crystal structure, and it many influences many properties of the material. Some of the commonly known dislocations that are present in a crystal structure are edge and screw dislocations, which are both shown in Fig. 2.5. An edge dislocation, Fig. 2.5(a) is a defect where an extra half-plane of atoms is inserted into the crystal structure. For a screw dislocation, Fig. 2.5(b) the crystal structure is sheared one-half the atomic distance without breaking any of the atomic bonds, creating a distortion in the crystal plane.

The magnitude and direction of the lattice distortion of the dislocation is often referred as the burgers vector, b. For an edge dislocation, the burgers vector is perpendicular to the lattice distortion, whereas for a screw dislocation, the burgers vector is parallel to the lattice distortion. The movement of dislocations through the crystal lattice is governed by two mechanisms known as either glide or climb. When a dislocation glides, the dislocation moves in the sample plane as burgers vector, often

referred as the slip plane. When a dislocation climbs, it moves out of the slip plane, normal to the direction of the burgers vector. For a dislocation to climb, the crystal lattice must be thermally activated to promote diffusion of an extra plane of atoms into the dislocation. At high temperatures, dislocations will have the ability to climb. At low temperatures where diffusion is unlikely, the movement of dislocations is primarily limited to glide.

These dislocations also provide a mechanism for atoms to move and allow for permanent and/or plastic deformation. The ease with which a dislocation migrates in a crystal structure also affects the hardness of a material. A large number of defects, however, will interact and prevent movement of the dislocations. An example is a line defect traveling through the material that stops because of a point defect. That point defect will prohibit the line defect from continuing its movement, acting as a pinning site. This will stop the material from plastically deforming, which in turn makes the material harder.

The number of point defects present in a crystal lattice influences the hardness of a material. This technique is widely used for many metal modifications. One of the most common is carbon steel. By adding carbon to iron, the carbon migrates into the iron crystal lattice as an interstitial and changes the hardness of the iron.

Similar to interstitials, voids, bubbles, and precipitates also have similar effects on the hardness of a material. A void is a collection of vacancies in the crystal structure, and bubbles are voids filled with a substitution gas. A precipitate is a void filled with a cluster of substitutional atoms different from the crystal lattice. Voids and bubbles can

cause the material to visibly swell due to the interior volume displaced. Voids, bubbles and precipitates, if in the path of a moving dislocation, make it hard for dislocations to traverse the material, thereby making it harder.

A grain boundary is often referred to as an interface between to misoriented single crystals in a polycrystalline solid. The grain boundary has properties that correspond to the hardness of a material. Grain boundaries make it difficult for a dislocation to move from on grain to another. In order for the dislocation to continue its path in the other grain, more energy is needed to initialize the dislocation at the new crystal orientation. By increasing the density of grains in a material, it has the ability to make the material harder.

Ion irradiation affects the numbers of defects that can be introduced into the material. These defects change the hardness of the material; this is known as irradiation hardening. In irradiation hardening, there are two mechanisms, source hardening and friction hardening. Source hardening is when the radiation damage locks an existing dislocation into place. Friction hardening is when the radiation damage creates several defects in the material and these defects impede the dislocation from moving. The only way for the dislocation to overcome the defect is by cutting through it or climbing over it. Fig. 2.6(a) illustrates an edge dislocation cutting though an obstacle; an obstacle is any type of defect that is in the path of a moving dislocation.

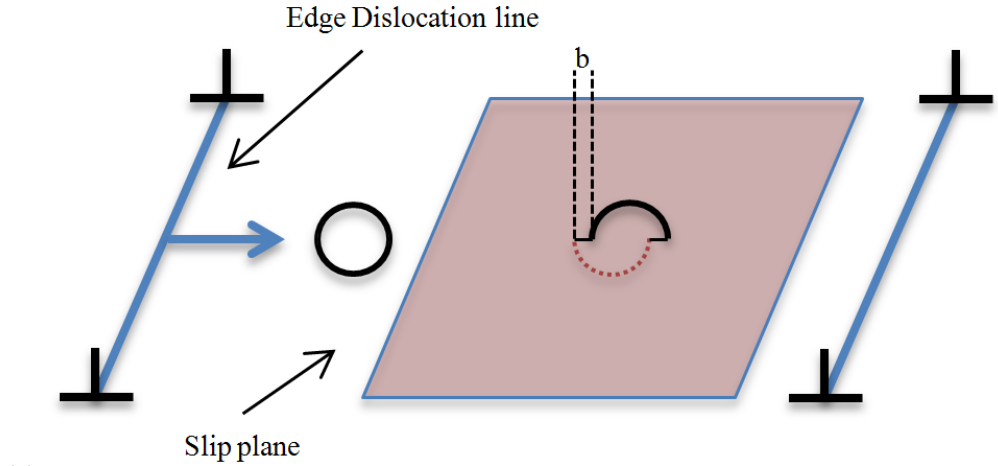

(a)

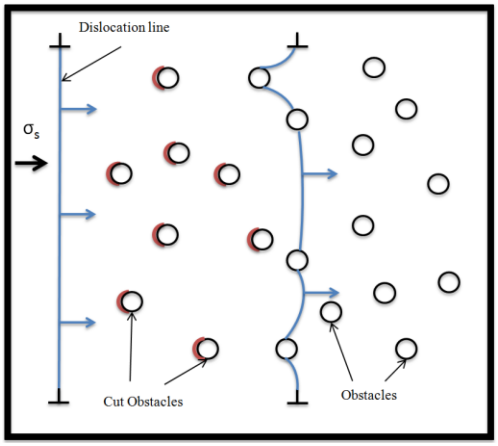

(b)

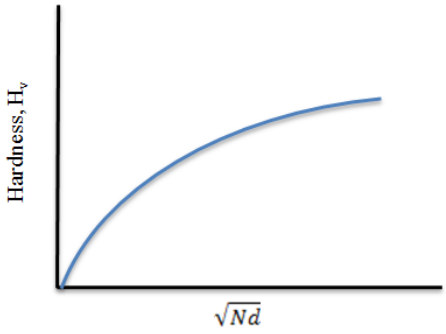

(c)

Figure 2.6: (a) Illustration of an edge dislocation as it moves along the slip plan and cuts an obstacle. (b) Slip plan with several obstacles randomly dispersed, as an edge dislocation migrates though it. (c) Represents the Vickers hardness as a square root function of the density and diameter of obstacles in a solid.

To better understand the effect of obstacles have on the hardness a relationship must be established to relate the hardness of a material to the density and diameter of an obstacle. These obstacles are considered to be spherical with a diameter, d, which are randomly distributed throughout the solid at a density of N cm^{-3}. The dependence of the diameter and the density of obstacles can be related to the hardness of a material given by Eqn. 2.10, where H is the hardness and ω is a constant that represents variables specific to the material.

$$H \propto \omega\sqrt{Nd} \ . \tag{2.10}$$

To derive the relationship in Eqn. 2.10, first relate the line tension from an edge dislocation, Γ, given by Eqn. 2.11 to the sheer stress, Eqn. 2.12,

$$\Gamma = \frac{\mu b^2}{4\pi} \ln\left(\frac{R}{r_c}\right) \tag{2.11}$$

$$\sigma_s = {}^{\Gamma}/_{bR} \ . \tag{2.12}$$

From Eqn. 2.11 and Eqn.2.12, R, is the grain radius, r_c is the dislocation core radius and dislocation core energy, b is the burgers vector, and μ is the shear modulus. To relate Eqn. 2.11 and 2.12 to the density and diameter of an obstacle, one must set to R= l /2. Where the product of the number of intersections per unit area, Nd and the square of the distance between obstacles, l^2 is unity, yielding the distance between obstacles $l = \frac{1}{\sqrt{Nd}}$. Then by substituting Eqn. 2.11 into Eqn. 2.12, is then be simplified to Eqn. 2.13, where α is a constant equal to $\alpha = \frac{1}{2\pi} \ln\left(\frac{l}{2r_c}\right)$.

$$\sigma_s \approx \alpha\mu b\sqrt{Nd} \tag{2.13}$$

From equation 2.13, the sheer stress then is related to the yield stress, σ_y of the material by a Taylor factor, M such that, $\sigma_y = M\sigma_s$, thus yielding equation 2.14,

$$\sigma_y = \alpha M \mu b\sqrt{Nd}. \tag{2.14}$$

Then from observations reported by P.Zhang et al.[9], yield stress is proportional to the hardness and, thus, creating the relationship between $H \propto \omega\sqrt{Nd}$.

From this derivation, there exists a model where there is a dependence on the density and diameter of obstacles and its relation to the hardness of the material, by a square root function. Figure 2.6(b) is an illustration of several obstacles in a slip plane. Figure 2.6(c) represents the Vickers hardness of a material as its dependence of the square root of the diameter and density of obstacles.

3. MOLECULAR DYNAMICS SIMULATION

3.1 Molecular Dynamics

Molecular Dynamics (MD) is a computer simulation method with the ability to model the physical movement of atoms under various different potentials for time scales on the order of pico to nanoseconds. The movement and trajectories of atoms are done by numerically solving Newtonian equations for interacting particles with a given potential energy. The scale of the simulation of an MD simulation in both time and volume allowed is limited by the computing power available. To run a simulation with millions of atoms, super computers are needed. Each individual atom is indexed and calculated during each iterate. This technique is computationally expensive; however, it results in an accurate movement and behavior for each individual atom. MD simulation has been widely used for work in chemical physics, material science and modeling for bimolecular studies.

Figure 3.1 is a flow chart that shows the MD simulation procedure. Initially, all the positions, velocities, and boundary conditions are defined. Next, the forces are calculated with parameters set by the simulation, and then the particles move according to the set of forces over a time step. This process will loop until the simulation reaches the end time.

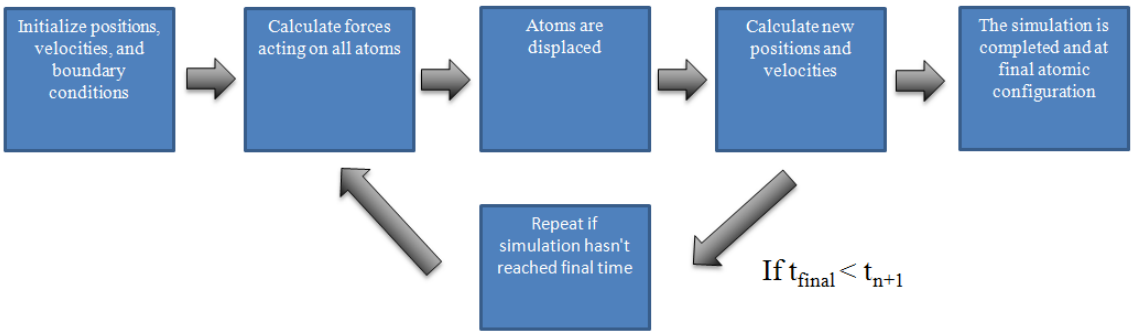

Figure 3.1: The simulation proceeds of molecular dynamics simulations.

A critical component of MD is the accuracy of interatomic potentials. The accuracy of the MD simulation is heavily determined by the accuracy of these potentials. Most potential values come from either quantum mechanics or empirical methods, however, there are also semi-empirical methods which combine elements of empirical and quantum calculations. Such potentials are used to determine the forces acting on pairs, or even large numbers, of particles on each other.

Quantum mechanics and ab-initio methods are used to calculate potentials. These potentials are created by solving multi-body Schrödinger equations. The advantage of using ab-initio methods is its accuracy. This method is based on first principles and usually gives the most accurate representations of inter-atomic potentials, however, it is very computationally expensive.

Empirical potentials represent quantum mechanical effects without solving the Schrödinger equations. The interatomic potentials are calculated using previous known data from either experiments or computations. This method is computationally

favorable, but is less accurate. Because semi-empirical potentials are a mixture of quantum mechanics calculations and empirical representations, semi-empirical potentials can offer a more accurate potential than a purely empirical method without the computational cost of the ab-initio calculations.

One of the critical potentials calculated from any of the methods above is the pair potential. Pair potentials describe the total potential energy between two atoms. A good example of a pair potential is the Lennard-Jones potential, which is mostly used to calculate Van der Waals forces. For some simulations, the pair potential of two interacting particles is not enough to give an accurate depiction of the forces acting on the atom, and the forces of other atoms need to be taken into account. In this case a Multi-body potential must be used. Multi-body potentials occur when the potential energy is a function of multiple atoms interacting with each other. A good example of a multi-body potential would be the Tersoff potential. This potential gives the total potential over groups of three atoms, where the angle between atoms is taken into account.

LAMMPS (Large-scale Atomic/Molecular Massively Parallel Simulator) is a classical molecular dynamics code. It can model atomic, polymeric, biological, metallic, granular, and coarse systems by using an assortment of different potentials and boundary conditions. LAMMPS was developed to make MD simulations simpler to setup and run. The US Department of energy under the Cooperative Research and Development Agreement developed this code which is now distributed by Sandia National Labs. The

current version of LAMMPS is written in C++ and designed to run on single or parallel processors.

The core mechanics of LAAMPS integrate the forces given by Newton's equations of motion over the simulated set of atoms. LAAMPS calculates this, while taking into account boundary and initial conditions set by the simulation. LAMMPS specialized in parallel computing, by using spatial-decomposition techniques to allocate different parts of the simulation into small sub-domains. These sub-domains then get assigned to an individual processor. Each processor has a specific output that corresponds to the simulation, where the final output can be easily constructed. By using this parallel method, LAAMPS is able to efficiently run the simulation and decrease computational time drastically by being able to use as many processors as are available.

3.2 Method of MD Simulation

The effect of ion implantation on tungsten is important to understand due to its proposed use as a PFM. For this study, MD was used to create a computational model to understand the basic principles of the dependence of void density and void diameter to the hardness. Ion implantation changes the hardness of a material by introducing defects into the crystal lattice [10,11]. For the purpose of this study, the defects introduced into the simulations were voids. By varying the void size and the void density, this gave a qualitative understanding on how these voids changed the hardness of tungsten.

The basis of this simulation was to recreate the Brinell hardness test. The size of the simulation was 12.6nm x 12.6nm x 9.5nm, which gave a test sample of 96000 atoms. An Embedded-Atom Method (EAM) potential was used. EAM is an approximation describing all energies between two atoms and all of its neighbor's potentials, and specifically designed for metals with a simple close packed structure. The system was heated up to 300K under the NVT ensemble, in which moles (N), volume (V), and temperature (T) were conserved. The time step for the simulations was 0.02 picoseconds (ps). The speed of the indenter was 0.02 angstroms ps^{-1} into the surface, until the indenter tip reached 2nm. Then, the indenter was pulled out at 0.02 angstroms ps^{-1}. In order to calculate the hardness of the material, Eqn. 3.1 was used.

$$H_b = \frac{2P}{\pi D(D-\sqrt{D^2-d^2})} \tag{3.1}$$

Where D, is the diameter of the indenter, d is the diameter of the indent, and P is the force on the indenter. Figure 3.2 is an illustration of the parameters used to calculate the, Brinell hardness, H_b.

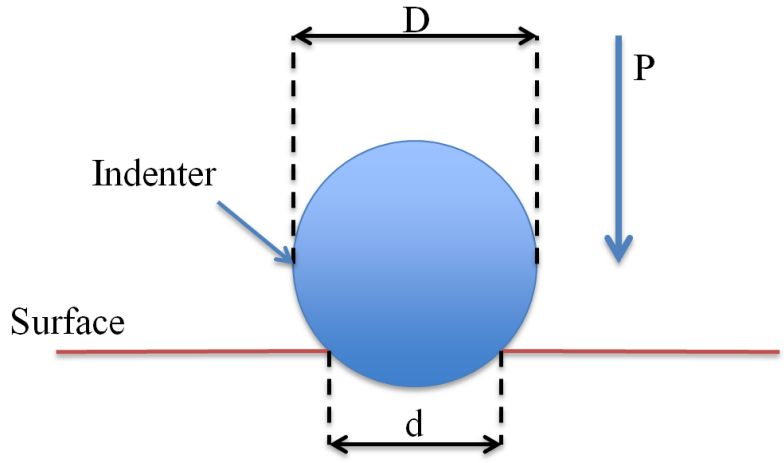

Figure 3.2: Illustrates the parameters used for the Brinell hardness test.

For the first simulation, a nano-indent in defect free tungsten was created in order to understand the basic properties of the tungsten, and to have a comparison to the other simulations. The next simulation was used to look at the dependence of void diameter on the hardness of tungsten. The void density was held constant, by creating a simulation that varies the void diameter, while holding the total volume of constant. All the voids were all placed on the atomic plane 4.5 nm away from the surface. This was done in order to create enough distance for the indenter tip to come in and not interact directly with the voids. This simulation is illustrated in Fig. 3.3(a).

The next simulation was used to look at the dependence of void density on the hardness of tungsten. The voids were randomly dispersed in the volume at a distance of 4.5 - 6.5 nm away from this surface. The void diameter for the simulation was set to 1 nm. The overall void density was then controlled by the number of voids created. This simulation is illustrated in Fig. 3.3(b).

As soon as the indenter comes in contact with the surface, a force was applied to the system of atoms in the simulation. The indenter will continue to apply a force until the tip of the indenter reaches 2nm into surface, and then the indenter will withdraw itself from the surface. For these simulations the tip of the indenter will take 1ns for it to reach 2nm.

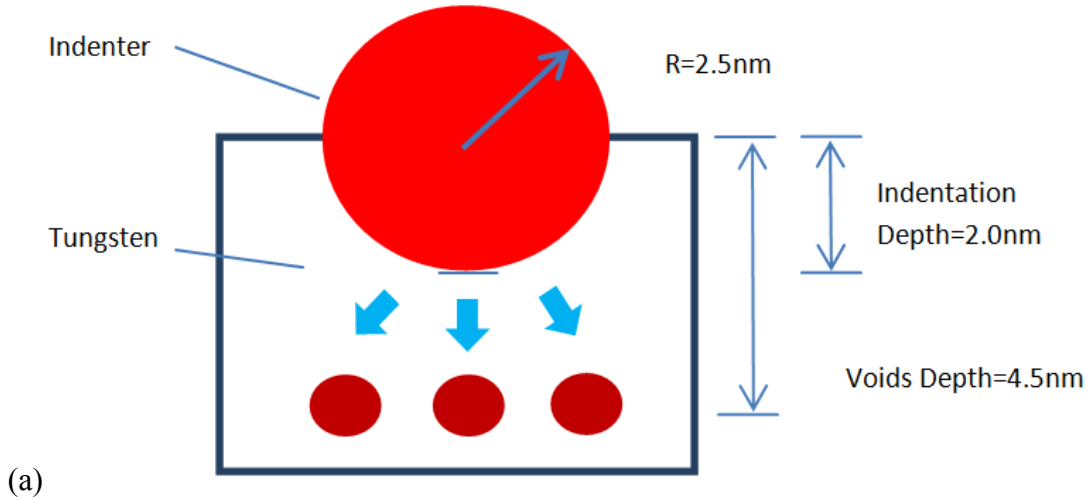

(a)

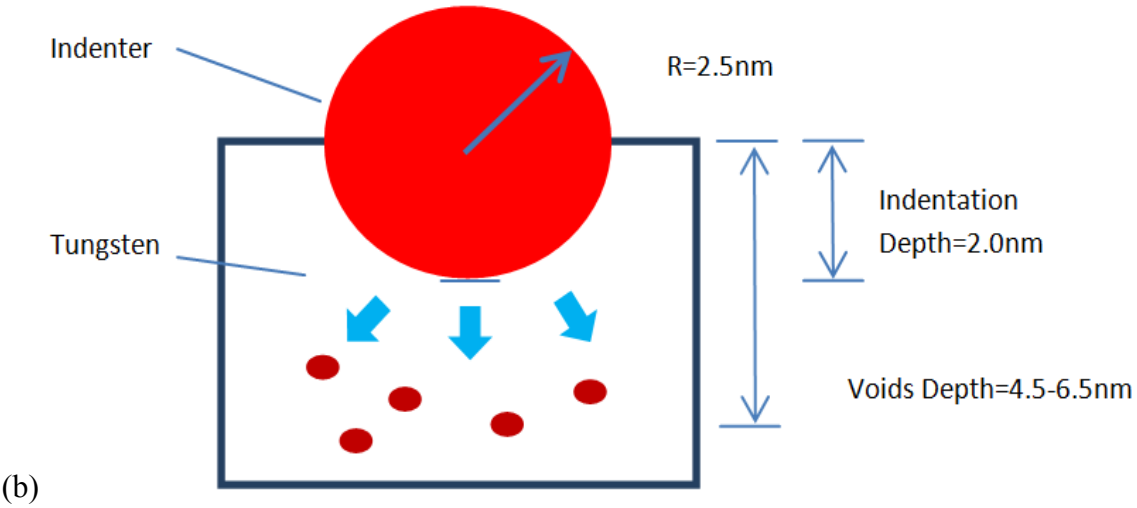

(b)

Figure 3.3: The parameters of each of the simulations, (a) where the dependency of diameter was investigated (b) where the dependency of density was investigated.

As the indenter applies a force into the system of atoms, the atoms experience a strong shear stress, and in order for the indenter to penetrate deeper into the system, several atoms will be displaced. The displacement of these atoms creates point and line defects within the system. The atoms near these defects experience a difference in their interatomic potential due to the stress field that surrounds the defect. From this data it is possible to look at the change of the interatomic potential and understand what types of defects are created in the simulation. By visually watching the simulation, the movements of potentials indicate the movements of line defects. This visualization will lend an understanding of how the defects will move and interact with the void region in each of the simulations.

To be able to calculate the hardness from these simulations, the force applied on the indenter, and the diameter of indent was extracted. From this knowledge, H_b can be calculated. From these calculations, a trend then could be discovered.

3.3 MD Simulation Results and Discussion

In this section, the data from the two simulations are presented. From the relationship that was in Section 2.2, where the dependence on the density and diameter of the obstacles was a square root function to the hardness. The hardness data extracted from these simulations should both follow that function.

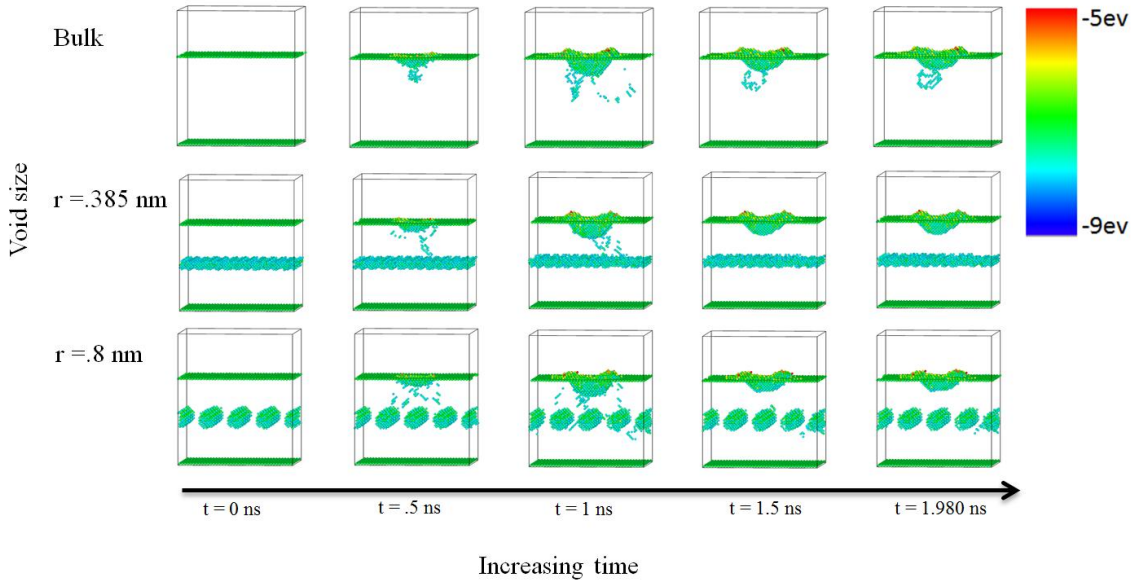

(a)

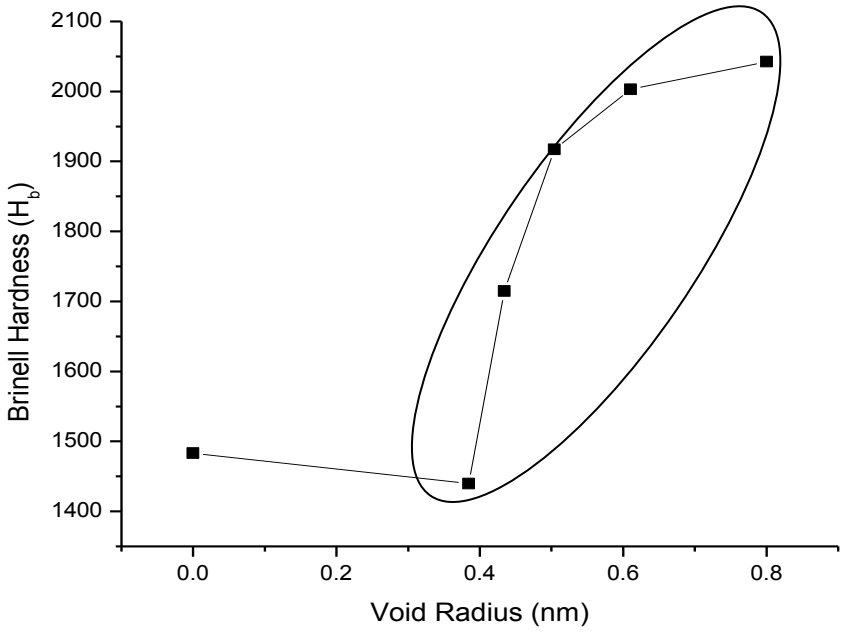

(b)

Figure 3.4: Results from MD simulation where the dependency of density was investigated. (a) an illustration of the time evolution of the simulations, and (b) is the H_b verses the void radius.

Figure 3.4 was the results from the first MD simulation, where the dependency of the void diameter was investigated. When examining Fig. 3.4(a), it is clear that defects are being created from the indenter and these defects migrate parallel to the force from the indenter tip. When observing the defect free simulation in Fig. 3.4(a), the defects that were created migrated from the indenter, and at the end of the simulation these defects were still present. In the other two simulations, the migrating defects interacted with the voids, causing the defects and voids to be partially removed through re-combination.

This was explained from the theory proposed back in Section 2.2, where an edge dislocation would travel along the slip plane, and interacts with an obstacle. If the edge dislocation were to have enough energy, it would cut the obstacle. From this simulation, such obstacles were voids, and if an edge dislocation where to come in contact with the void with enough energy to cut through the void. Then extra half plane of atoms from the dislocation would then be injected to volume of the void. Depending on the size of the void, injection of atoms from the extra half plane could then remove this defect. This becomes more evident under close examination of this simulation.

In Figure 3.4(b), the plot of the H_b verses the void radius; it becomes evident when looking at the last four points of the plot that it follows a square root function. This result was expected, due to the relationship between obstacle density and diameter in Section 2.2. However, when looking at the second point from the plot, when then radius of the void was 0.385nm; it seems as if there was a slight decrease in hardness. This behavior is not expected, but could be explained by the constraints of the simulation.

From this simulation, the total void volume was kept constant to preserve the overall void density of the simulation. If the void radius was too small, several voids are created in order to preserve the density of voids. However, there becomes a critical point where too many voids are created and for the simulation, and all these small voids are placed on a single plane. Thereby, increasing the localized density of voids to a point where the voids interconnect and form a porous structure. The mechanics for line defect interaction with porous structures are completely different than that of an independent obstacle. A line defect will preferentially migrate toward a porous structure since it is an easy pathway to release the energy in a line defect. This, in turn promotes defect mobility, decreasing the hardness of the material. Also there is some irrelevance to compare a system that tests the dependence of void diameter to a system of no voids. There is a fundamental difference between the mechanics of the two systems. This constraint to the simulation explains the slight decrease in hardness shown in Fig. 3.4(b).

Figure 3.5 was the result from the second set of MD simulations, where the relationship between hardness and void density of tungsten was investigated. Fig. 3.5(a) and 3.4(a), shows the same properties of defect creation and defect migration from the indenter. It was clear to see that by increasing the total number of voids, the systems total void density could be controlled.

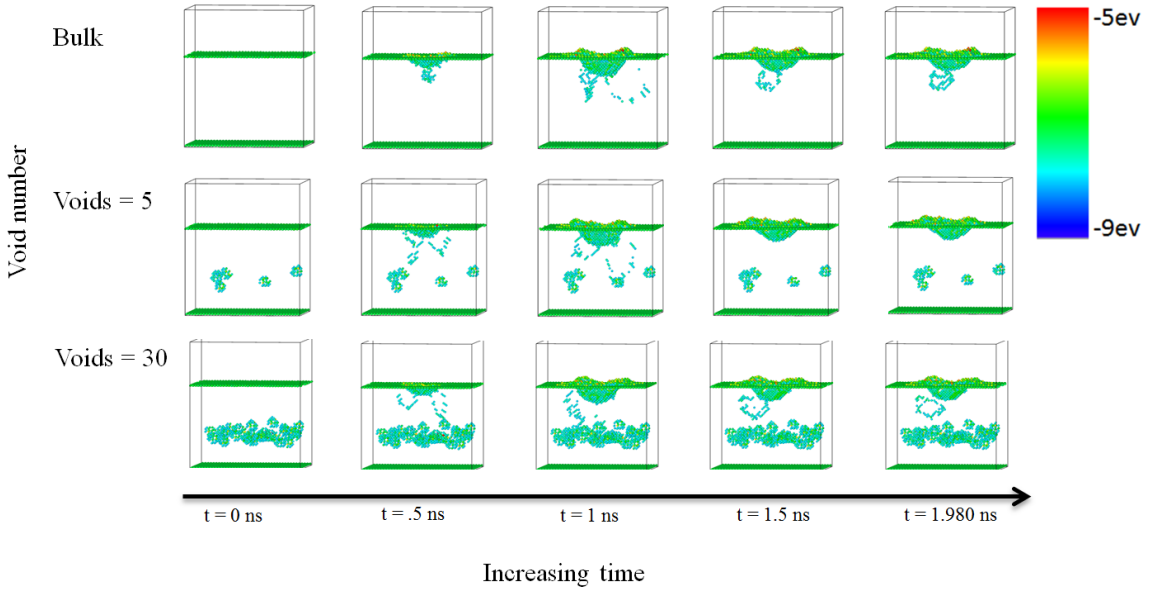

(a)

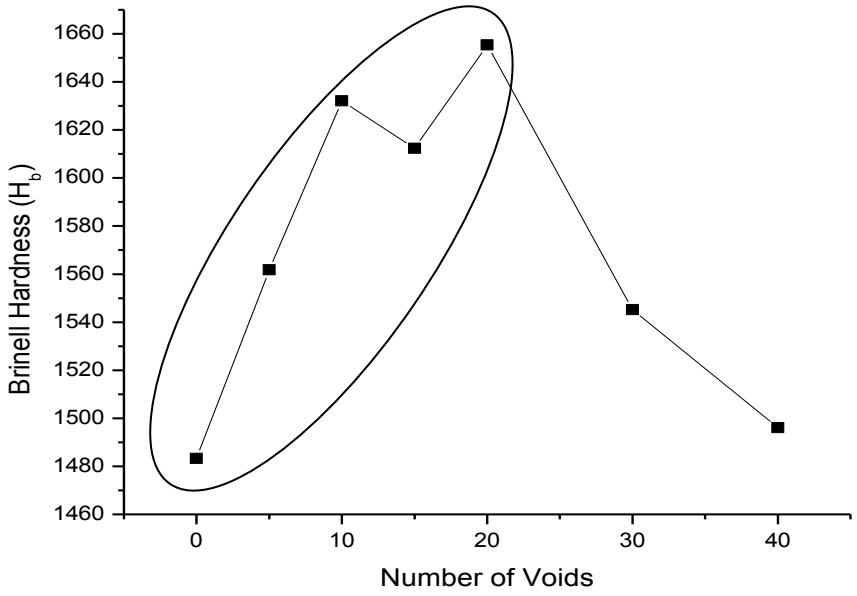

(b)

Figure 3.5: Results from the MD simulation where the dependency of the density was investigated. (a) an illustration of the time evolution of simulations, and (b) the H_b verses the number of voids in the system.

By observing Fig. 3.5(b), the first five points in the plot; there is a positive correlation between void density and hardness, which resembles a square root function. The result that was expected to follow a square root of because of the dependence stated in Section 2.2. For last two points in Fig. 3.5(b), the hardness decreased with the increase increasing void density, which doesn't fit the expected trend. This could be explained by the constraints of the system. It was mentioned prior that, there was a critical point where if the localized void density was too high in a certain region, the void region will act as a porous structure rather than an obstacle. This becomes more apparent when comparing the localized void density for the simulation with 30 and 40 voids present. For these two simulations the overall void density was high and acted as a porous structure

When looking at the fourth point in Fig. 3.5(b), it becomes clear that there is a slight inflection to the trend. This could be explained by how the voids were introduced into the simulation. The voids in the simulation were randomly placed in a region between 4.5 - 6.5nm, the configuration of how these voids were placed have an effect on line defects that are interacting with it. If two obstacles were placed close together the dislocation would have a harder time to cut through both of them due to the close proximity of the obstacle and the associated forces that surround it. For these regions with a close proximity of obstacles, the localized hardness value would be much higher than the surrounding regions. For this simulation, the voids were all randomly placed; therefore, the hardness value could vary even with the same number of voids present due to variance in the localized hardness.

4. MICROSTRUCTURAL AND MECHANICAL CHANGES IN ION IRRADIATED TUNGSTEN

4.1 Introduction to Irradiated Tungsten

To understand the effect of irradiated tungsten it is important to know the basic properties of pure tungsten. In raw form, tungsten is a brittle, but very hard metal with a steel gray appearance. It has a high melting point (3,422 ^{o}C), an exceptional tensile strength of 1501 MPa, and its atomic crystal structure is body-centered cubic (BCC), it has a low sputtering yield, and high thermal conductivity. These properties make it an ideal candidate as a PFM in a fusion reactor.

The effect of radiation on tungsten has been mostly focused on characterizing its ability to withstand the harsh environments of a fusion reactor. Copious amount of research has been conducted to understand the effects of individual irradiation of H and He [12-32], and the resulting changes of the surface morphology [5,20,28]. Also, many have individually studied the individual diffusion of He and H in tungsten [14,17,22,29,31]. However, there has been little research undertaking to understand the mechanical property changes that are associated with any ion irradiation. The key part of this study was to be able to co-implant He and H at a deep enough level where accurate measurements of the mechanical properties could be recorded.

Though the focus of this thesis is different from past studies, the previous work offers a preliminary understanding of how tungsten will react to ion irradiation and the diffusion of He and H [7,9]. From previous studies it is seen that He will cause major changes in surface morphology, including blisters, as well as extensive nano-bubble

formation [24,26,30]. H, on the other hand, will migrate deep into the material, and preferentially exists in the tetrahedral interstitial site and at grain boundaries [15,18]. Some studies have also has offered insight on how both H and He affect each other's retention and migration in the material [3,5]. From these previous works, it gives a predicted behavior of what could be expected in a H and He co-implantation of tungsten, and could offer an explanation of some of the mechanisms seen in this experiment.

4.2 Experiment Instruments

Use of a linear particle accelerator was pivotal in this experiment. A particle accelerator is a complex machine used to produce, accelerate, manipulate, and finally implant energetic ions into a given sample. There are many different methods for producing ions, for example: electron and chemical ionization, gas discharge ion sources, desorption ionization, and spray ionization to name only a few of the techniques used to produce the charged particles needed for the ion beam. Each source type has its own unique strengths and weaknesses. The source simply has to be chosen so the desirable ion species can be produced at the necessary rate. The ion beam is then accelerated and steered by electrostatic and electromagnetic forces to the sample implantation stage.

The amount of energy an ion beam has is determined by two factors: the charge state of the ion and the electric potential of the acceleration column. The amount of energy is described in terms of electron volts (eV), which is defined as the kinetic energy of a single elementary charge as it moves across an electric potential difference of one

volt. For example, an ion with a single elementary charge passing through an electric potential field of 100 volts, gains 100eV of energy. Since the eV energy unit is relatively easy to calculate from known machine parameters, it is used frequently in this field to refer to the energy of an ion.

Another important aspect of ion acceleration is the total number of ions deposited per area, known as fluence. By knowing the beam current, which is directly proportional to the number of ions that are interacting with the sample per second, the fluence can be measured by integrating the beam current over a period of time. The ion fluence in the sample is a critical quantity since it is directly proportional to the total amount of energy deposited. Another critical requirement to ion acceleration is that the entire accelerator system must be kept at high vacuum conditions, typically around 10^{-7} torr. In order to maintain such vacuum conditions, a combination of turbo, diffusion and ion pumps are placed throughout the accelerator system. If a high vacuum environment is not maintained, the ions could never reach the target due to interactions with the gas atoms in the beam line.

4.2.1 140KV Ion Accelerator

The H and He implants were performed using a 140KV single-ended accelerator, at the Ion Material Faculty at Texas A&M University. A 3-D computer model of the complete accelerator system is represented in Figure 4.1. The accelerator is equipped with a Danfsick ion source with the capability of producing ions from both gaseous and solid material.

During operation, the filament must reach a critical temperature in order to ionize the input gas and create plasma. Inside the source there is a tungsten filament that is heated by passing a high electric current through it; at a high enough temperature, thermal electrons are emitted from the filament. The filament is surrounded by an anode; this anode is positively biased so that the electrons that are being emitted from the filament are drawn towards it. Once the gas enters the source, through an operator-controlled leak valve, it interacts with the electrons being emitted from the filament. The electron knocks off one of the orbital electrons from the gas atom, making it positively charged. The knocked off electron is then pulled by the potential gradient toward the anode where it has the possibility to interact other gas atoms. This process, if started relatively far from the anode, can create a cascade of electrons and ionized gas particles atoms. The gas atoms that have interacted with the electrons create positively charged plasma.

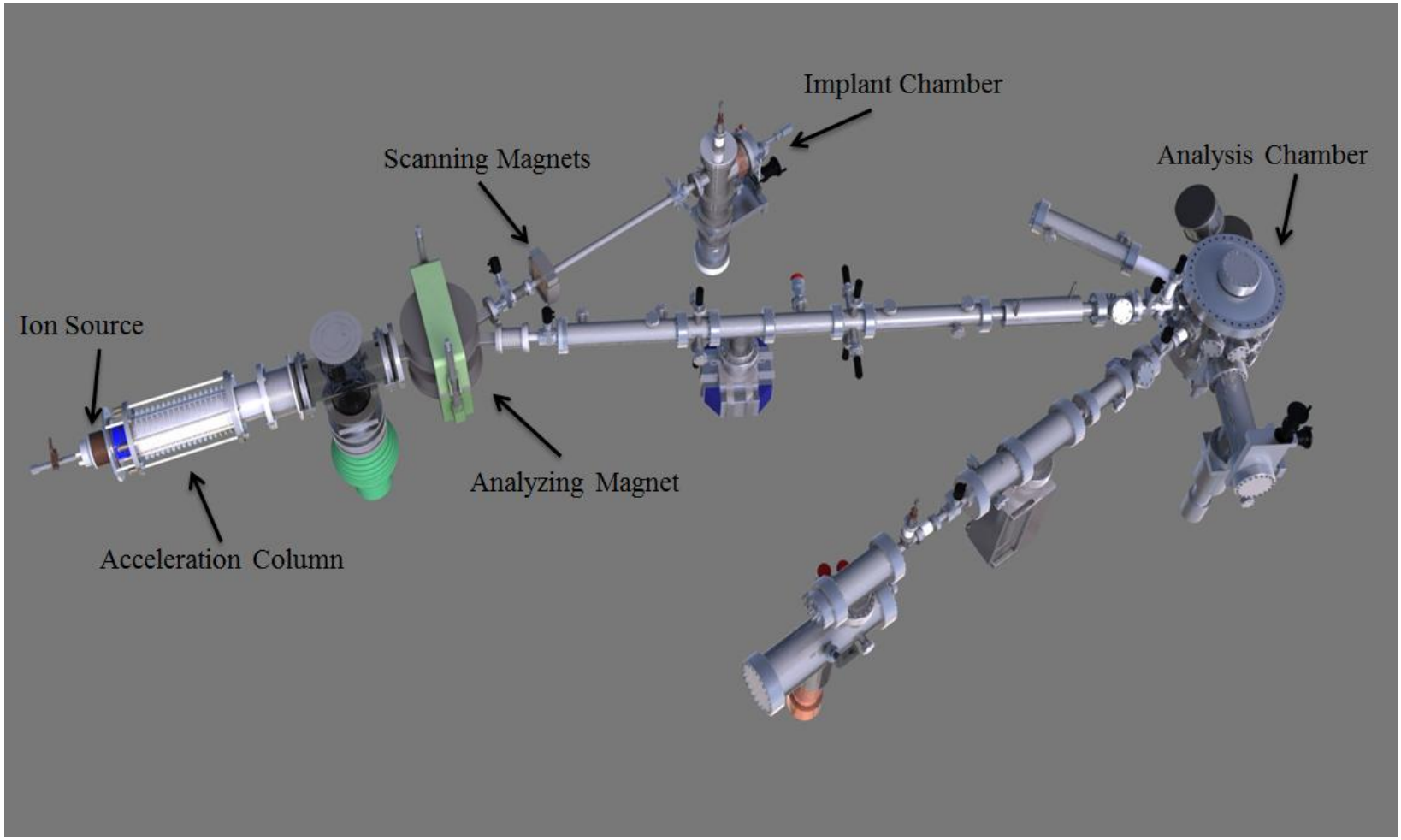

Figure 4.1: A 3D model of the 140KV ion accelerator at Texas A&M University. From the ion source the ion travels through the acceleration column, gains energy and then passes through the analyzing magnet, where it could bend to one of the two beam lines present. For this experiment the ion travels to the implant chamber.

To extract the plasma a voltage bias is placed across the plasma, creating a potential gradient to drive the ionized atoms out of the source. Once the plasma is extracted, it passes through an Einzel lens where an applied voltage is used to focus the plasma into a beam. After the ion beam leaves the lens it then passes through the acceleration column. The acceleration column consists of several chevron shaped plates in series. The accelerating voltage potential is applied across the column creating a voltage gradient which will determine the energy of the exiting particle. After the beam leaves the acceleration column it reaches the glass cross. On the bottom leg of the four-way cross, a diffusion pump is used to keep the source and magnet volumes at a high vacuum level. The system base pressure is around $1x10^{-7}$torr, which is read by an ion gauge located near the glass cross.

The ion beam then enters the analyzing magnet. The analyzing magnet is used to filter out any unwanted ion species or charge states that may exists in the ion beam. The analyzing magnet is an electromagnet, where a power supply finely controls the current, which, in turn, controls the magnetic field strength of the magnet. Once the magnet is tuned to the proper magnetic field strength, the ion beam will then bend accordingly to the mass to charge ratio. If there were any unwanted ion species in the ion beam, these species would bend at a different rate due to a difference mass to charge ratio compared to the desired ion species. The ion beam under the proper settings has to bend at a 15^{o} angle to travel toward the implant chamber.

After the 15^{o} bend, the ion beam then passes through another set of magnets, known as steering magnets. These magnets are controlled by a bipolar operational

power supply and which gives the ability to steer the beam vertically and horizontally. This allows the operator to place the beam precisely onto the target in the implant chamber. In order to implant an area, the magnets that were used to steer the beam onto the target are connected to a wave function generator to scan the beam across a desired area. These wave generators control the power supplies for the steering magnets, causing the ion beam to move from left to right and bottom to top in a random pattern, thereby taking the ion beam with a beam spot of about 5mm in diameter, and scanning it over an area about 1-2cm^2. In this chamber, the sample is placed and irradiated. A turbomolecular pump, pumps down the pressure to about $1x10^{-7}$ torr, and the vacuum pressure is read by an ion gauge.

The sample is attached to an electrically isolated target holder that has a bias of +135V for electron suppression. A small lead is connected to the target holder where it is able to read beam current, and fed to a current integrator which allows for the total charge collection to be accurately measured in-situ. Figure 4.2 is a 3D computer model representation of the scanning magnets and implant chamber.

Figure 4.2: Close up 3D model of the implant chamber and the scanning magnets.

4.2.2 Nanoindenter

A nanoindenter was used to measure the mechanical property changes induced by the irradiation. The nanoindenter that was used was for this experiment was a Hysitron TI 900 TriboIndenter, which is a low-load nanomechanical test system. This indenter is primarily used to test the hardness and the elastic modulus of thin films and coatings. Some key features of this machine are: automated testing, in-situ imaging, acoustic and thermal enclosure, top down optics, sub-micron resolution staging, and an active vibration dampening system. The various test methods it offers are quasistatic nanoindentation, scratch testing, and SPM imaging. Figure 4.3 is a picture of the nanoindenter used for the material testing for this experiment.

Figure 4.3: Photograph of the nanoindenter used for this experiment at Texas A&M University.

One of the major features of this nanoindenter is environmental isolation from such things as ambient acoustic noise, and air currents. Another key component of this system is the transducer, which gives the system very accurate readings of displacement. The displacement is measured by the change in capacitance of the transducer. As the indenter tip approaches the sample and pushes down with a small amount of force, the small inflection in capacitance is correlated to the depth of the tip into the material. These electrical signals are then sent to a program, where the data is analyzed and represented in terms of the mechanical properties.

The tip used for this experiment was a Berkovich tip. This tip is a short, but wide three-sided pyramid made of diamond. The Berkovich tip is mad out of diamond which is used for its hardness properties since the tip used must be harder than that of the material it is testing. This Berkovich tip is commonly used for measuring the properties of materials that have a thickness greater than 100 nm.

4.2.3 Imaging Instruments

TEM is tool used to take a micrograph of a high resolution sample on the atomic scale. This microscope uses an electron beam that passes through an electron transparent sample. The micrograph is formed by the interaction of the electrons that get transmitted through the sample. The electron beams interacts based on the density of the sample, the transmitted beam then gets magnified, and focused on a phosphorus screen. An image is then created on the phosphorus screen, based on the intensity of the electron beam. The contrast of this image is based the relative density of the sample, where lighter area indicate low density and darker areas high density. A TEM was used to observe the microstructural changes in tungsten.

A Scanning Electron Microscope (SEM) is a tool used to take a high-resolution micrograph of sample surface topography. SEM uses a bulk sample and an electron beam that raster scans the sample and then analyzes the secondary electrons that are coming from the surface. These secondary electrons are generated when the electron beam comes in contact with the surface of the material. As electron beam raster scans across the sample, and the position of the electron beam is mapped to the output of the secondary electron detector. The intensity of the signal from the secondary electron

detector and the position is known, and from this output, an image of the surface topography can be constructed. This was used for this experiment to characterize the surface morphology of the tungsten samples.

A Focused Ion Beam (FIB) is a tool that is used for understanding the site-specific analysis, deposition, and ablation of materials. A FIB has the ability to finely focus a beam of ions onto the sample. Low ion beam currents are used for imaging and at high beam currents the FIB can be used for sputtering or milling. This system gives the ability to cut electron transparent sample, which then can be analyzed by using a TEM. A FIB was used to create cross-sectional TEM samples.

4.3 Experimental Setup and Procedure

This section will outline the experimental procedures and setup for this study. The tungsten samples used for this experiment were 99.95% pure tungsten, purchased from Alfa Aesar. These tungsten samples were cut into 1mm thick discs, and then mechanically polished to a mirror finish to remove any surface defects. The samples were irradiated at the Ion Materials Facility (IMF) at Texas A&M using the 140 KV particle accelerator described previously. Table 4.1 contains the sample matrix and the corresponding fluence that each sample received.

Table 4.1: Represents the sample matrix that will be used for the following experiment.

Sample #	Fluence (He ions/cm^2)	Fluence (H ions/cm^2)
1	1.00E+15	0
2	1.00E+16	0
3	3.00E+16	0
4	7.00E+16	0
5	1.00E+17	0
6	1.00E+15	1.00E+15
7	1.00E+16	1.00E+15
8	3.00E+16	1.00E+15
9	7.00E+16	1.00E+15
10	1.00E+17	1.00E+15
11	0	0

From Table 4.1 samples 1-5 were only irradiated by He, and samples 6-10 irradiated with He with a small fluence of H. The He implants were irradiated with 140KeV He^+ ions, and the H implants were irradiated with 75KeV H_2^+, both irradiations were at room temperature. SRIM has predicted that a 140KeV He^+ ion will have an R_p of about 270nm, and the 75KeV H_2^+ ion will have an R_p of about 150nm. Figure 4.4 shows the range distribution for the He and H implants, Fig. 4.4(a) and 4.4(b), respectfully. During every irradiation session, the vacuum pressure was near 1 x 10^{-6} torr, and the scanned ion beam area was approximately 1cm^2.

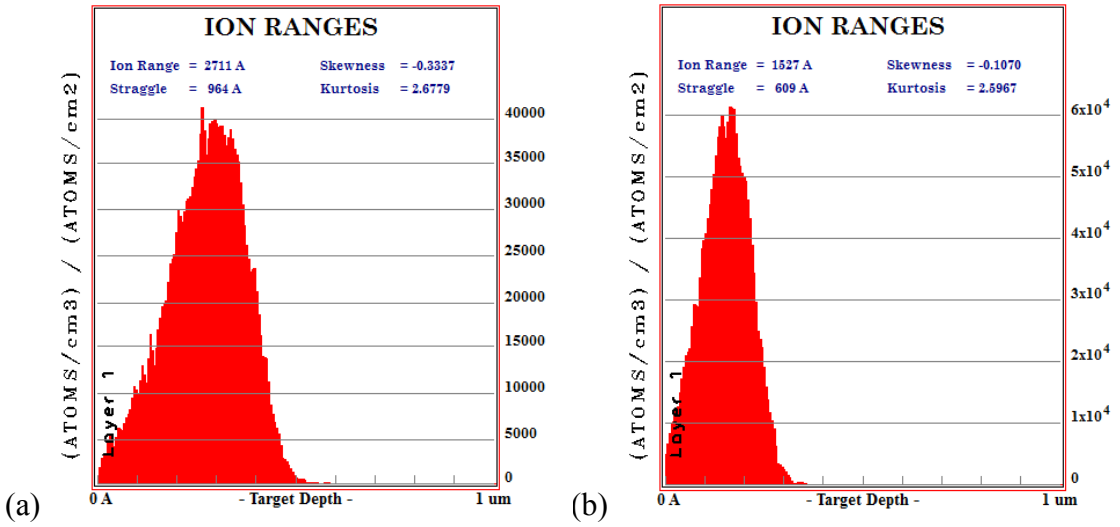

(a) (b)

Figure 4.4: The ion ranges calculated by SRIM, (a) the ion range of 140KeV He^+ and (b) the ion range of 75KeV H_2^+..

The first feature about the implant depth noticed, is that the peak implant regions do not line up. This was done intentionally so the different effects on microstructure due to H and He effects could be observed separately. If the two ions were at the same R_p, the H will preferentially be trapped in the heavily damaged region of the He implant [16], and it will difficult for the H to diffuse into the bulk and have other interactions. By having an interface, the two different species have the opportunity to diffuse into the interface and demonstrate the interaction H and He have.

After the irradiation, micrographs of the surface morphology were taken by using a JEOL JSM-6300 at the Microscopy & Imaging Center (MIC) at Texas A&M University. Micrographs were taken pre and post irradiation to observe the changes in the surface morphology of the samples. A 15 KeV electron beam was used with a working distance of 25mm. The samples were tilted away from the secondary electron

detector about 30^{o} degrees, in order to accentuate the surface morphology. From these settings, micrographs were taken of each sample. Then these samples were brought to the Materials Characterization Facility (MCF) at Texas A&M University, for nanoindentation. Each sample was tested on the Hysitron TI 900 Triboindenter and the mechanical properties where then recorded.

Two samples were then sent to Idaho National Laboratory (INL). The chosen samples were: the sample which received a fluence of 7×10^{16} of He^{+} ions and the sample which received a fluence of 7×10^{16} of He^{+} ions plus 1×10^{15} of H_2^{+} ions. There a Focused Ion Beam (FIB) was used to create a cross-sectional TEM sample. The process used to create the cross-sectional TEM sample was an *in situ* lift-out (INLO) technique. This technique cut two trenches, one on each side of the sample, thereby leaving a thin electron-transparent portion. This electron-transparent portion was then removed from the bulk sample and placed on a TEM grid. Once both of the tungsten samples were placed on TEM grids, they were shipped back to Texas A&M University for further characterization.

The two samples were then examined using the FEI TECNAI G2 F20 ST FE-TEM at the MIC at Texas A&M University. Using a 200KeV electron beam, micrographs were taken at the implanted region at various magnifications to look for changes in microstructure.

4.4 Results and Discussion of Mechanical and Microstructural Changes

The first results from the co-implantation of H and He into tungsten, was the dependence of fluence to the hardness of tungsten. Table 4.2 shows the matrix of the samples that were irradiated with the corresponding fluence to the hardness data from the nanoindentation.

Table 4.2: Represents the fluence of He^3 and H_2^+ ions that each sample received and its corresponding hardness after irradiation.

Sample #	Fluence (He^3 ions/cm^2)	Fluence (H_2^+ ions/cm^2)	Hardness (GPa)
1	1.00E+15	0	8.35
2	1.00E+16	0	9.54
3	3.00E+16	0	10.28
4	7.00E+16	0	10.28
5	1.00E+17	0	10.23
6	1.00E+15	1.00E+15	8.75
7	1.00E+16	1.00E+15	9.81
8	3.00E+16	1.00E+15	11.18
9	7.00E+16	1.00E+15	11.18
10	1.00E+17	1.00E+15	11.48
11	0	0	7.6

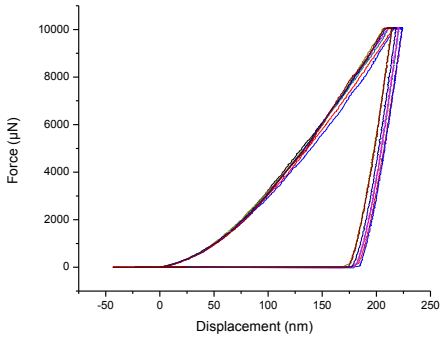

(a)

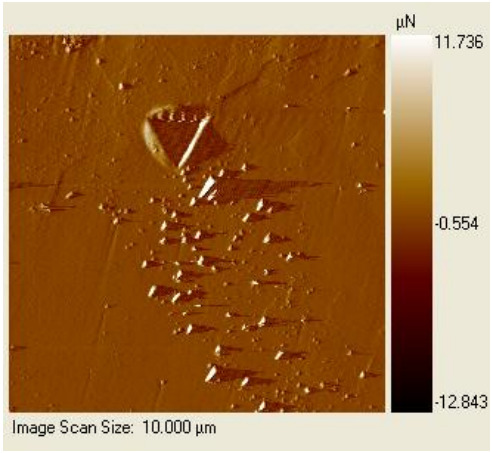

(b)

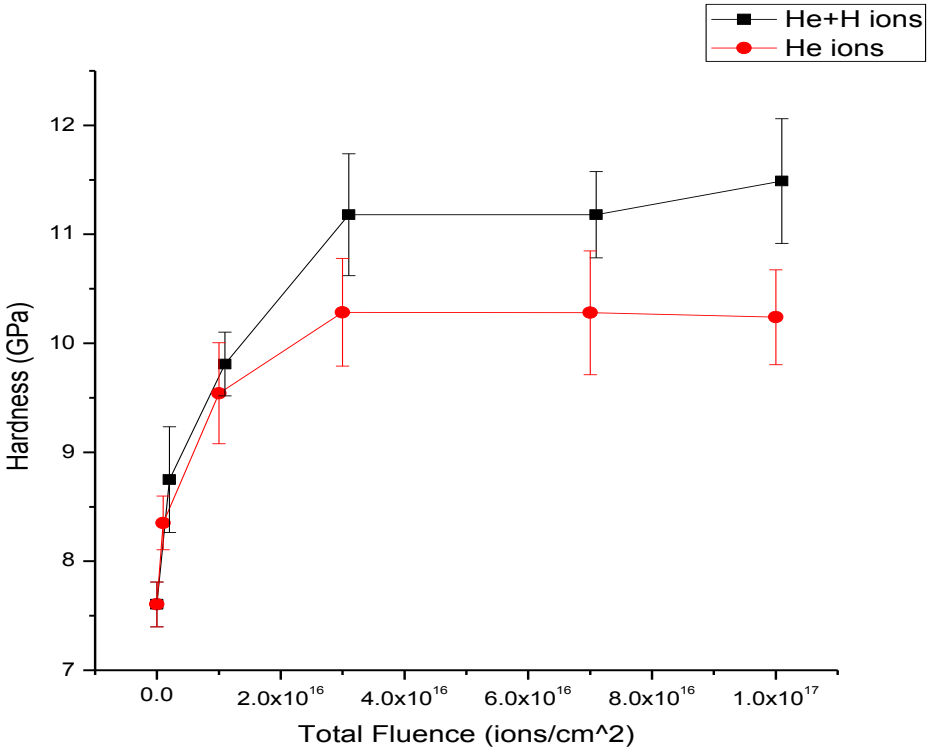

(c)

Figure 4.5: The data extracted from the nanoindenter, (a) the force verse displacement curve of a nano-indent of a sample that was irradiated, (b) the raster scanned image using the indenter tip of the indent at (a), and (c) a graphical representation of Table 4.2, with the associated error bars.

From Table 4.2 and Fig. 4.5(c) it was observed to see there was an overall increase in the hardness of the tungsten with an increase of fluence. The overall trend for this plot seems to accurately predict what was expected from Section 2.2, a square root function, as well as from the MD simulations performed. As the fluence increases, the amount of radiation damage in the material is proportional to the fluence, and the amount of radiation damage is related to the number of defects present in the material. Thereby increasing the fluence also increases such parameters that influence the material's hardness. However, the one observation is that the samples that were irradiated with H and He have a higher hardness value when compared to just a He irradiated sample.

The data from this experiment seems to suggest that the mechanism for increasing the hardness in tungsten is different for the co-implantation of He and H. Studies looking at He showed that the He tends to migrate towards vacancies and these vacancies are nucleation sites for He nano-bubbles [26,28,31].Thus there is an increase in the number of He nano-bubbles that are created in the material. These nano-bubbles, as mentioned in Section 2.2, will form obstacles for defect migration, increasing the hardness of the material. It should be noted that this effect is separate from the other point defects, also created by He, from implantation.

From previous studies irradiation using H, it showed that H atoms tend to prefer the tetrahedral interstitial site in a BCC crystal lattice [15,17]. Also H has the ability to stabilize the movement of vacancies in the material [17]. It is important to observe, that even with a small fluence of H compared to that of He, there was an increase in the

hardness value. This could be a result from nanoindentation testing method and two suspected mechanisms for hardening. The data from the nanoindentation suggest that the indenter tip penetrated about 200nm into the surface. The H implanted region was 150nm from the surface, and it the effect from the indenter tip coming in contact with the H implanted region could of affected the hardness. From the two distinct implanted regions in co-implantation of H plus He, there exists two regions that might affect the hardness property. H preferentially exists as an interstitial, from what was discussed in Section 2.2; interstitials affect the hardness of the material. These two mechanisms could explain why, there was a difference in the hardness between the He irradiated samples and the He plus H irradiated samples.

It was known that He irradiation causes a formation of bubbles and blisters at the surface [26-29]. Most studies observe these effects of tungsten at shallow implants of He or H [4,20,25]. These shallow implants only impacted the first few nanometers of material. Figure 4.6, shows SEM micrographs of the surface morphology of tungsten at various different at fluencies from this experiment.

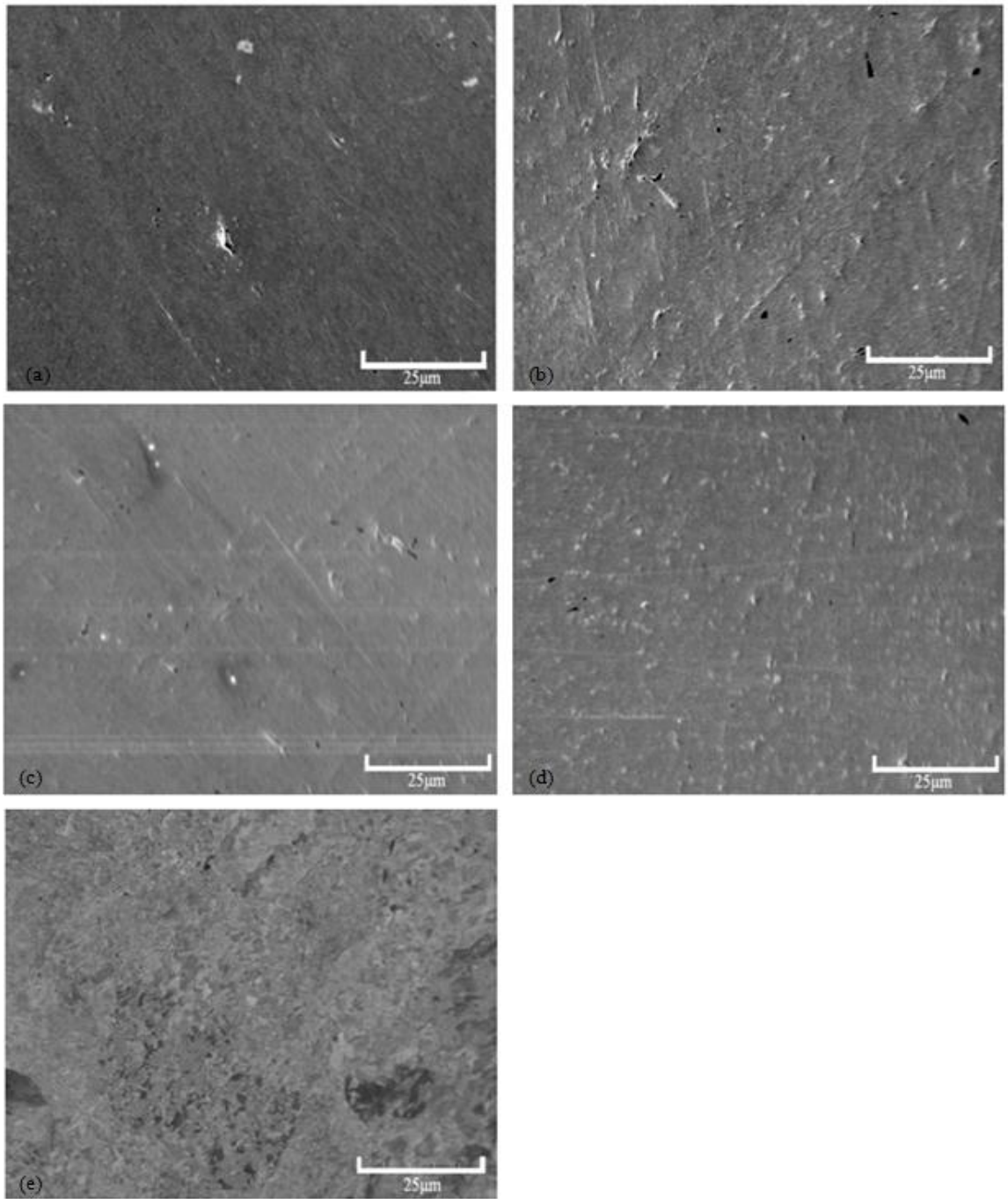

Figure 4.6: The surface morphology of the various samples that were irradiated. (a) was irradiated with 1 x 10^{15} $He^{+}cm^{-2}$, (b) was irradiated with 1 x $10^{15}He^{+}cm^{-2}$ and 1 x $10^{15}H_2^{+}cm^{-2}$,(c) was irradiated with 3 x 10^{16} $He^{+}cm^{-2}$, (d) was irradiated with 3 x 10^{16} $He^{+}cm^{-2}$and 1 x 10^{15} $H_2^{+}cm^{-2}$, and (e) was unirradiated.

When observing Fig. 4.6, it becomes apparent that the unirradiated sample Fig. 4.6(e) and comparing it to the others micrographs in Fig 4.6, that there are major differences in the surface morphology. When comparing the differences between the surface morphology and the fluence, it was evident that with increasing fluence, more defects were created on surface [4]. However, when comparing the surfaces of the Fig. 4.6(a) and 4.6(c) to Fig. 4.6(b) and 4.6(d), there are vast differences in the surface morphology to a small fluence of H. From previous studies that studied shallow implants, the closer the implant was to the surface, the more the drastic the change in the surface morphology. This drastic change was mainly due to the shallow depth of bubble formation in those studies [28]. For this experiment, H was implanted much closer to the surface than He, and this resulted for there to be more surface defects. This because more apparent when observing Fig. 4.6(b) and 4.6(d). In these two figures the surface morphology is approximately equal since the H fluence is about the same, even though the He fluence was drastically different.

Figure 4.7(a) shows a micrograph of the unirradiated region of the tungsten sample that was co-implanted with H and He, it is clear from that micrograph that it is polycrystalline tungsten. This region is microns away from the implanted region and has no radiation induced defects. Fig. 4.7(b), shows a micrograph of the unirradiated region in tungsten only irradiated with He. From Fig. 4.7(a), the crystal structure is exactly what was expected for the observation of unirradiated region [30]. From figure 4.7(b), this distinctly shows a different structure. For this sample the parallel lines that are present in the grains, is an artifact from mechanically polishing. These lines are edge

dislocations moving down the grain, in order to relieve the stress from the surface from the mechanical polishing. However, this artifact did not have any influence on the irradiated region or interfered with the results from the nanoindentation.

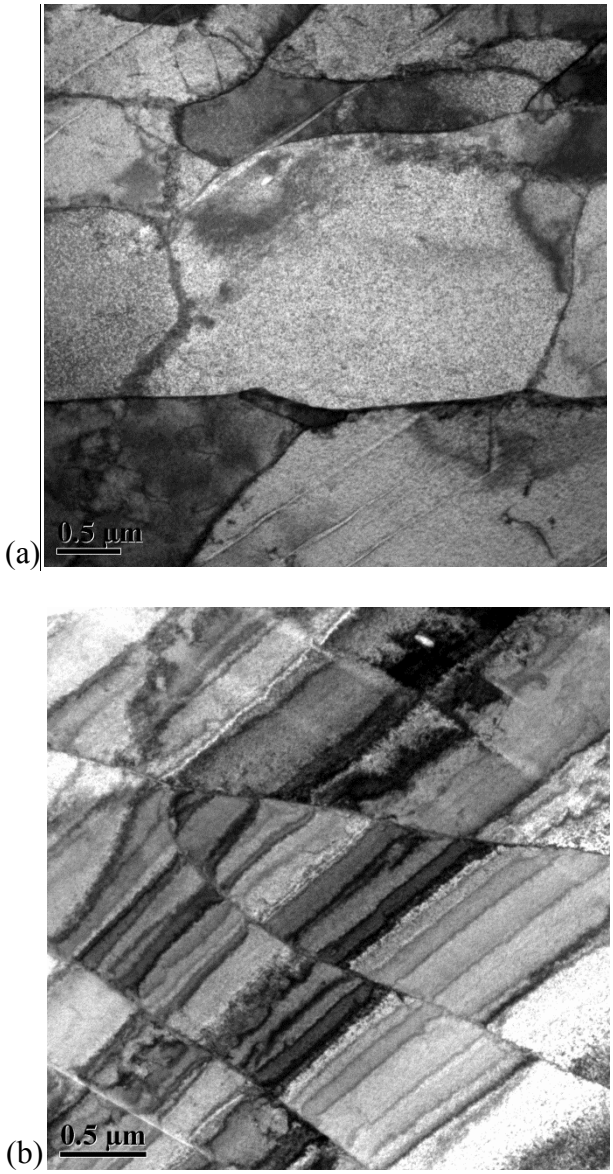

Figure 4.7: Cross-sectional TEM micrographs of tungsten,(a) a micrograph of the unirradiated region from sample of that was irradiated by 7 x 10^{16} $He^{+}cm^{-2}$ and 1 x 10^{15} $H_2^{+}cm^{-2}$, and (b) a micrograph of the unirradiated region from sample that was irradiated by 7 x 10^{16} $He^{+}cm^{-2}$.

Fig. 4.8 represents a series of micrographs taken from the He irradiated sample. The implanted region for H is about 270nm from the surface. The micrographs Fig. 4.8(a) and 4.8(b) were both taken from this region, and Fig. 4.8(c) was taken at the interface between the sample surface and the implanted region. From the observations of the implanted region in Fig. 4.8(a), there are He nano-bubbles present in the grain boundary and scattered throughout the region. This type of formation was expected from the results from many different experiments [15,22,33]. Also it is clear to see that the implanted region is heavily decorated with a high density of defects, these defects consist of dislocation loops, and a high density of other dislocations. Fig. 4.8(b) would suggest that not only He preferentially migrates towards vacancies; it also preferentially migrates to grain boundaries and is a nucleation site for He nano-bubbles [33]. When observing Fig. 4.8(c), the interface between the sample surface and the irradiated region, that there is a gradient of radiation damage that progress toward the irradiated region. Figure 4.8(d), captures the overview of where these micrographs where taken. The radiation damaged area seen is roughly 270nm from the surface, exactly where the SRIM predicted the R_p of the 140KeV He^+ ion would be.

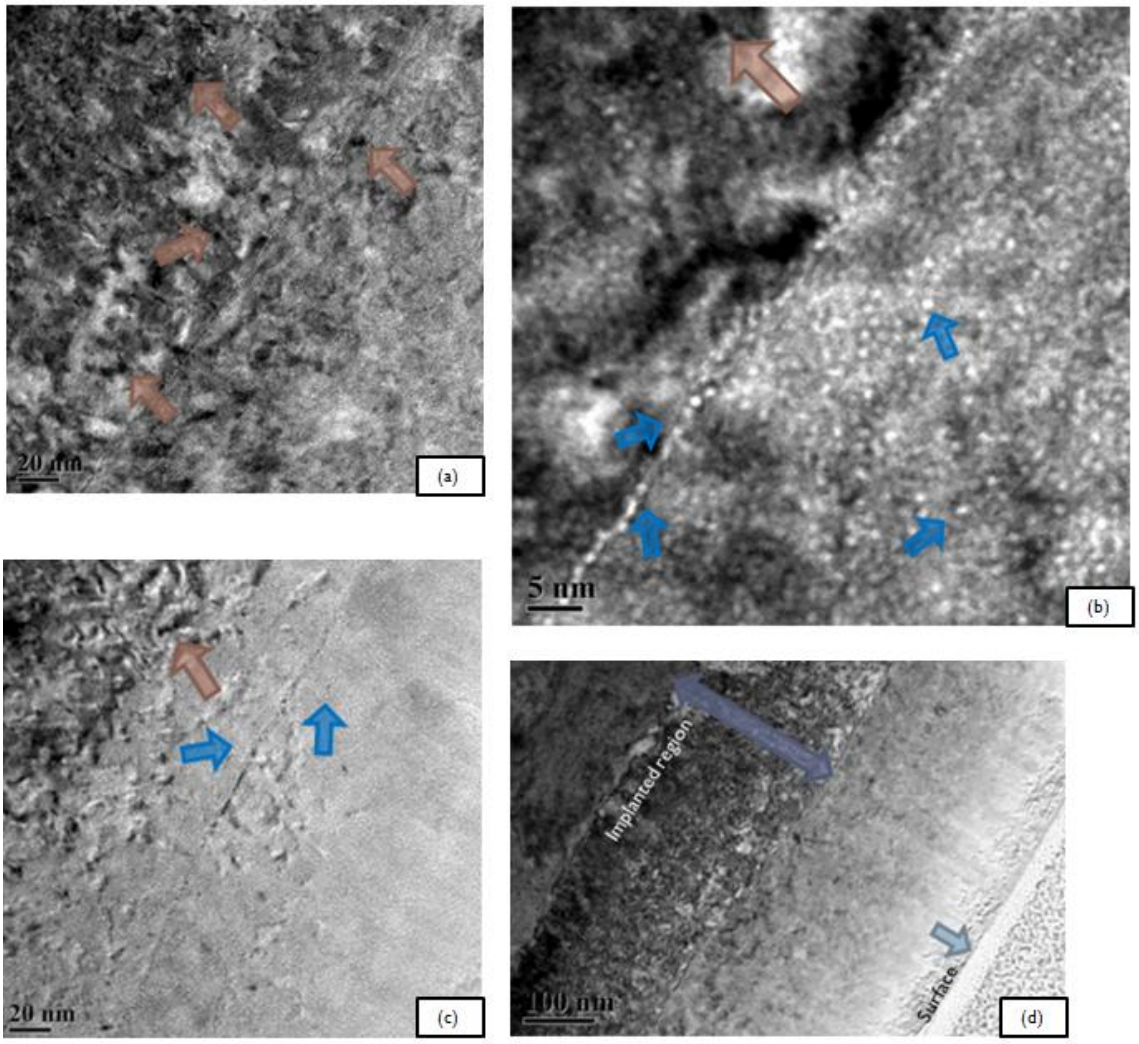

Figure 4.8: Cross-sectional TEM micrographs of 7 x 10^{16} $He^{+}cm^{-2}$of irradiated tungsten at the implanted region, where brown arrow signify dislocation loop and bright blue arrow signify He nano-bubble. (a) a micrograph at the implanted region, (b) a close up micrograph of Fig 4.8(a) at a grain boundary,(c) a micrograph of the interface between the surface and the implanted region, and (d) an overview of the area where these micrographs were taken.

When comparing to the unirradiated tungsten, Fig. 4.7(a) to Fig 4.8(d), the microstructure between the two are vastly different. These defects from radiation damage and He nano-bubbles are the obstacles that block the movement of dislocation which was discussed in Section 2.2. From these changes in the microstructure, the creation of He nano-bubbles and the radiation damage present, are the mechanisms that leads to the changes in the mechanical properties of tungsten.

Figure 4.9 are micrographs taken from the TEM cross-section of the sample that was co-implanted by He and H into tungsten. Fig. 4.9(a) captures the two distinct regions of the radiation damage from both implants. The damaged region on the left hand side was from the H irradiation, and the damaged region on the right was from the He irradiation.

Figure 4.9(b), is an overview of the cross-section sample, this region was where the other micrographs were taken. Under further investigation the He irradiated region seems to disappear. The reason for this was because that there were uniformity issues in the creation of the cross-sectional TEM sample.

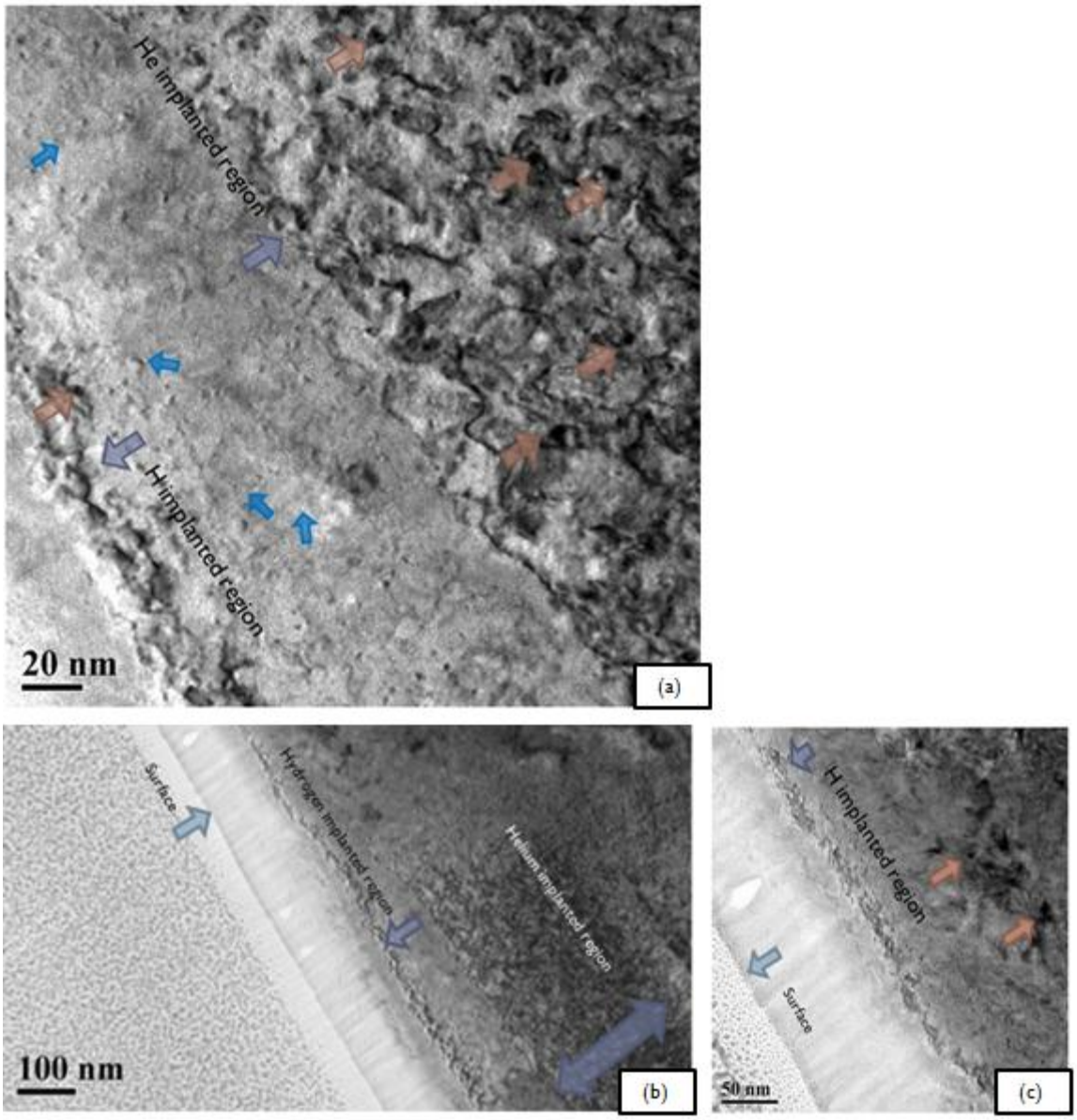

Figure 4.9: Cross-section TEM micrographs of 7 x 10^{16} $He^{+}cm^{-2}$ and 1 x 10^{15} $H_2^{+}cm^{-2}$ of irradiated tungsten at the implanted region, brown arrow signify a dislocation loop and bright blue arrow signify a He nano-bubble.(a) a micrograph at the implanted regions of He and H, (b) an overview of the sample where these micrographs were taken, (c) a micrograph from surface to the He implanted region.

During the process to make the cross-sectional TEM electron transparent, sample was aggressively thinned in this region, supplying sufficient energy for the irradiated region to re-crystalize. Also another artifact to support that the sample was incorrectly prepared was that when observing Fig. 4.9(b), the first 100nm away from the surface has a very bright contrast from the rest of the material, indicating an uneven thickness throughout the sample. The presence of holes near the surface, not produced by ion implantation also lends evidence to this theory. Another artifact was the presence of dislocation loops and radiation induced defects artifacts that at the He implanted region, but it does not correspond to the appropriate radiation damage seen in the other areas of the sample.

Under close inspection, it would seem apparent that there are some He nano-bubbles formed were formed in the interface region in Fig. 4.9(a). However, when comparing it to Fig. 4.8(c), the density of He nano-bubbles was greater. This becomes more apparent when looking at Fig. 4.10 (a) and (b) which are magnified versions of the micrographs from Fig. 4.8(c) and 4.9(a) respectively. After post image processing of Fig. 4.10(a) and 4.10(b), using a blob detector, it identified the suspected He nano-bubbles and indicates their presence by putting a box over it. Figure 4.10(c) and 4.10(d) are the respected Fig. of 4.10(a) and 4.10(b). From these images it becomes apparent that there are different mechanisms that govern the formation of He nano-bubbles in a H and He co-implanted tungsten.

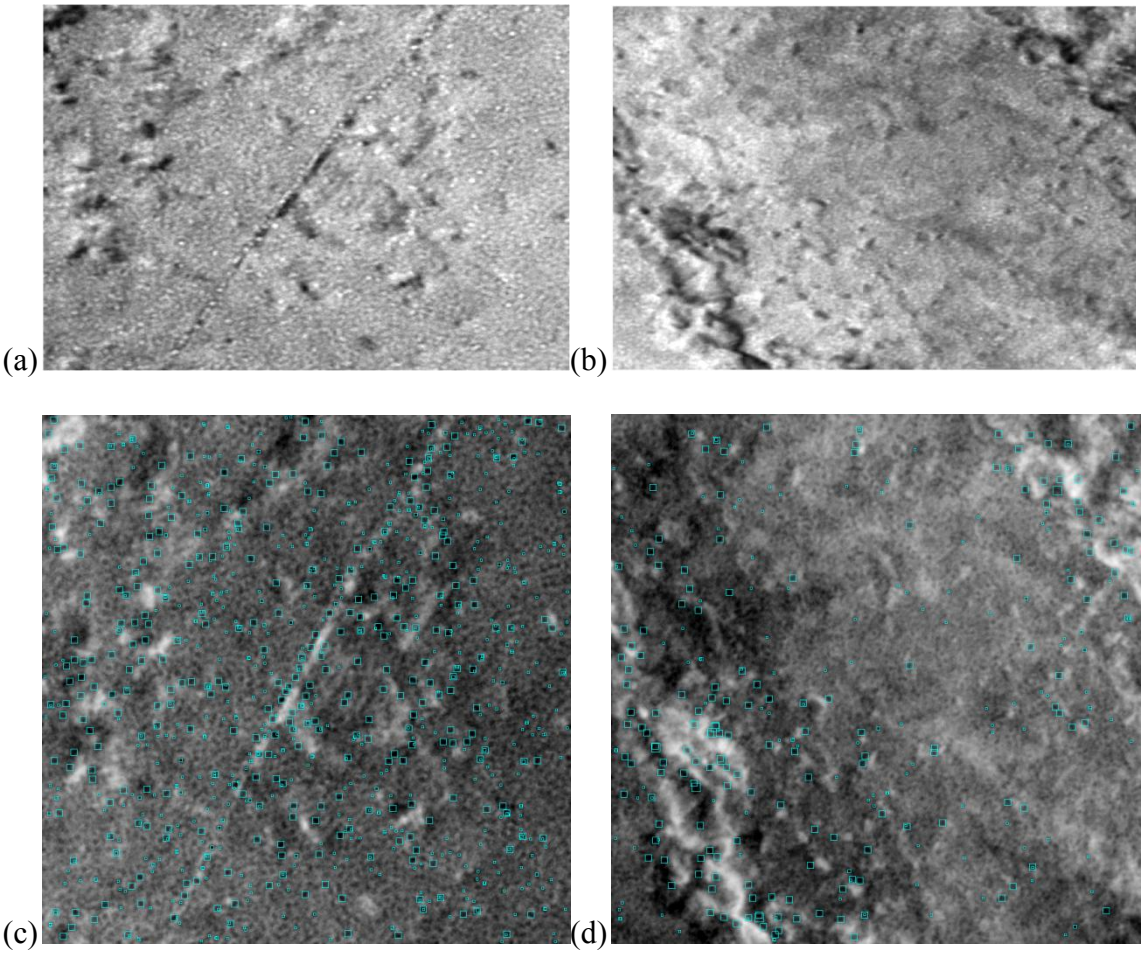

Figure 4.10: Magnified micrographs to accentuate the location of He nano-bubbles for the blob detector, (a) was irradiated by He, (b) was co-irradiated by both He and H, (c) post image processing of the He irradiated sample, and (d) post image processing of co-irradiated He + H.

The lack of He nano-bubbles in the co-implanted H + He sample could be explained by a mechanism proposed by Kirsanov and Musina [34]. In this paper, computer simulations showed that, the permeability of He is crucial to the formation of He nano-bubbles. In the crystal, He will migrate and fill a vacancy (V) and form (He + V) cluster. The permeability of He is now dependent on the (He + V) cluster and subsequent He and vacancy clusters. The (He + V) cluster is relatively immobile, but with the addition of another vacancy, this can initialized the movement of He. Thus the (He + V) + V cluster becomes mobile within the crystal. From this mobility of the (He + V) + V cluster, it migrates in the crystal, traps more He, and, thus, creating a nucleation site for He nano-bubbles. The mobility of the (He + V) + V cluster is the driving mechanism for the nucleation of He nano-bubbles.

However, if H is present, it will fill the other vacancy, thus creating (He + H + 2V) cluster. This cluster then becomes immobile, however the dissociation energy to remove H from the (He + H + 2V) cluster is relatively low. Once the energy of the system is high enough, the H will be knocked out and (He + V) + V cluster will be formed, and, thus, the mobility of (He + V) + V through the crystal is regained. From H interaction, it plays a major role in the permeability of He through the crystal.

From their work, it becomes clear that with the interaction of H and He in tungsten is an important factor, and that this mechanism greatly affects the nucleation of He nano-bubbles. Their work clearly defines a mechanism that could explain the differences in the number of He nano-bubbles created in the He irradiated sample and the H + He co-implanted sample.

5. CONCLUSION

The work that was presented in this thesis has offered valuable information where there has been no previous investigation. Through the MD simulations and the co-implantation of H and He on tungsten, it has offered a basic model to explain the relative changes of hardness from such effects that are present as a PFM.

In Section 3, an MD simulation was used to simulate the characteristic changes of hardness in tungsten. The simulation recreated a Brinell hardness test on tungsten. Once the simulation was created, voids where then introduced into the system to look at the dependency of the void radius and void density to hardness. These results predicted that both of these factors would follow a square root function to the change of hardness. Also the movement of dislocations and its interaction with voids were investigated, and it was observed that edge dislocations had the ability to remove voids from the system. When interpreting the data from the simulations, it becomes apparent that it follows predictions.

In Section 4, the co-implantation of H and He into tungsten was conducted. The characterization of the post irradiated samples was studied, focusing on the changes of mechanical properties and microstructure of the post irradiated samples. The mechanical property that was investigated for this study was the hardness. The results match what was predicted; fluence was dependent on the relative hardness of tungsten, which followed a square root function. Also, the data suggested that with a small fluence of H, it has the ability to slightly increase relative hardness of tungsten. This was explained by the conditions of the experiment, where there exist two irradiated

regions in this sample, and that the H region came in contact with the nanoindenter tip and could have perturbed the results.

The changes in microstructure after irradiation were then characterized by looking at cross-sectional TEM images of the post irradiated tungsten. One sample was irradiated only by He and the other sample was irradiated with the same fluence of He with an additional small fluence of H. Some features were seen in both samples, such as a dense region of defects from the subsequent irradiation and the creation of He nano-bubbles. However, under close inspection, it becomes apparent that there were more He nano-bubbles present in the sample that was only irradiated by He. The cause for such differences was the interaction that H has with the mobility of He as it moves though a solid. H has the ability to decrease the permeability of He in a solid, and as the nucleation of He nano-bubbles in tungsten is highly depended on the permeability of He. As a result, this lead to the difference in the number of He nano-bubbles observed between the samples.

The observations of MD simulations and results of the co-implantation of H and He into tungsten reflect the dependency of the defects in a material to the hardness of tungsten. However, the model presented is a basic way to explain such changes, and more work is needed to understand the governing principles for each mechanism. The work present in this thesis provides the first step into exploring the changes of mechanical properties regarding a co-implantation of H and He into tungsten, and suggest that the co-implantation of H and He must not be neglected when understanding the behavior of tungsten as a PFM.

REFERENCES

[1] V. Philipps, J . Nucl. Mater. **82**, S2 (2011).

[2] J. Paméla, G.f. Matthews, V. Philipps, and R. Kamendje, J. Nucl. Mater. **363-365**, 1 (2007).

[3] H. Iwakiri, J. Nucl. Mater. **307-311**, 135 (2002).

[4] K.Tokunaga , T. Fujiwara, K. Ezato, S. Suzuki, M. Akiba, H. Kurishita, S. Nagata, B. Tsuchiya, A. Tonegawa, and N. Yoshida, J. Nucl. Mater. **390-391**, 916 (2009).

[5] N. Enomoto, S. Muto, T. Tanabe, J.W. Davis, and A.A. Haasz, J. Nucl. Mater. **385**, 606 (2009).

[6] B.B. Cipiti, and G.l. Kulcinski, J. Nucl. Mater. **347**, 298 (2005).

[7] H. Lee, A. Haasz, J. Davis, and R. Macaulaynewcombe, J. Nucl. Mater. **360**, 196 (2007).

[8] B.I.Khripunov, A.N. Brukhanov, V.M. Gureev, V.S. Koidan, S.N. Kornienko, S.T. L.S. Danelyan, V.S. Kulikauskas, V.V. Zatekin, V.G. Vostrikov, and E.A. Romanovsky, J. Nucl. Mater. **415**, S649 (2011).

[9] P. Zhang, S.X. Li, and Z.F. Zhang, Mat. Sci. Eng. A-Struct. **529**, 62 (2011).

[10] G. Was, *Fundamentals of Radiation Materials Science: Metals and Alloys*. (Springer, Berlin, 2007).

[11] M. A. Nastasi, J. W. Mayer, and J. K. Hirvonen, *Ion-solid Interactions: Fundamentals and Applications.* (Cambridge University, Cambridge, 2004).

[12] W. Wang, J. Roth, S. Lindig, and C.h Wu, J. Nucl. Mater. **299**, 124 (2001).

[13] Z. Tian, J.W. Davis, and A.A. Haasz, J. Nucl. Mater. **399**, 101 (2010).

[14] M. Shimada, Y. Hatano, P. Calderoni, T. Oda, Y. Oya, M. Sokolov, K. Zhang, G. Cao, R. Kolasinski, and J.p. Sharpe, J. Nucl. Mater. **415,** S667 (2011).

[15] J. Xu, and Jijun Zhao, Nucl. Instrum. Meth. B. **267**, 3170 (2009).

[16] M. Fukumoto, H. Kashiwagi, Y. Ohtsuka, Y. Ueda, Y. Nobuta, J. Yagyu, T. Arai, M. Taniguchi, T. Inoue, and K. Sakamoto, J. Nucl. Mater, **386-388**, 768 (2009).

[17] Johnson, Donald F., and Emily A. Carter, J Mater. Res. **25**, 315 (2010).

[18] H. Zhou, Y. Liu, S. Jin, Y. Zhang, G.-N. Luo, and G-H. Lu, Nucl. Fusion. **50**, 10 (2010).

[19] A. Pisarev, J. Nucl. Mater. **220-222**, 926 (1995).

[20] R. Sakamoto, J. Nucl. Mater. **220-222**, 819 (1995).

[21] A. A. Haasz, M. Poon, and J. W. Davis, J. Nucl. Mater. **266-269**, 520 (1999).

[22] R.A. Causet, and T. J. Venhaus, Physica Scripta. **94**,9 (2001).

[23] S. Sharafat , A. Takahashi, Q. Hu, and N.m. Ghoniem, J. Nucl. Mater. **386-388**, 900 (2009).

[24] Q. Xu , N. Yoshida, and T. Yoshiie, J. Nucl. Mater. **367-370**, 806 (2007).

[25] D. Nishijima, J. Nucl. Mater. **329-333**, 1029 (2004).

[26] N. Yoshida, H. Iwakiri, K. Tokunaga, and T. Baba, J. Nucl. Mater. **337-339**, 946 (2005).

[27] D. Nishijima, M. Ye, N. Ohno, and S. Takamura, J. Nucl. Mater. **313-316**, 97 (2003).

[28] H. Iwakiri, J. Nucl. Mater. **283-287**, 1134 (2000).

[29] S. Gilliam, S.M. Gidcumb, N.R. Parikh, D.G. Forsythe, B.K. Patnaik, J.D. Hunn, L.L. Snead, and G.p. Lamaze, J. Nucl. Mater. **347**, 289 (2005).

[30] K.Tokunaga, R. Doerner, R. Seraydarian, N. Noda, Y. Kubota, N. Yoshida, T. Sogabe, T. Kato, and B. Schedler, J. Nucl. Mater. **313-316**, 92 (2003).

[31] S. Kajita, N.Yoshida, R. Yoshihara, N. Ohno, and M. Yamagiwa, J. Nucl. Mater. **418**, 152 (2011).

[32] P. Lhuillier, T. Belhabib, P. Desgardin, B. Courtois, T. Sauvage, M.f. Barthe, A.l. Thomann, P. Brault, and Y. Tessier, J. Nucl. Mater. **416**, 13 (2011).

[33] H. Zhou, Y. Liu, Y. Zhang, S. Jin, and G. H. Lu, Nucl. Instrum. Meth. B. **267**,3189 (2009).

[34] V.V.Kirsanov, M.V. Musina, and V.V. Rybin, J. Nucl. Mater. **191-194**, 1318 (1992).